Dynamic Control of Hippocampal Spatial Coding Resolution by Local Visual Cues

Romain Bourboulou[1,2], Geoffrey Marti[1,2], François-Xavier Michon[1], Morgane Nouguier[1], David Robbe[1], Julie Koenig[1,3] and Jérôme Epsztein[1,3,4]

1 Institute of Neurobiology of the Mediterranean Sea (INMED), French National Institute for Health and Research (INSERM UMRS1249), Aix-Marseille University, Marseille, France.

2 Equally contributing first authors

3 Senior authors

4 Lead contact

& correspondence

Drs Jérôme Epsztein or Julie Koenig

INMED/INSERM U1249

Parc scientifique de Luminy

163 route de Luminy

BP 13 13273

Marseille cedex 09

Tel: 00 33 4 91 82 81 47

jerome.epsztein@inserm.fr

Julie.koenig@inserm.fr

Abstract

Animals can flexibly navigate in their environment. This ability is thought to rely on an internal cognitive map. An open question concerns the influence of local sensory cues on the cognitive map and notably their putative contribution to setting its spatial resolution. Here we compared the firing of hippocampal principal cells in mice navigating virtual reality environments in the presence or absence of local visual cues (virtual 3D objects). Objects improved the spatial representation both quantitatively (higher proportion of place cells) and qualitatively (smaller place fields with increased spatial selectivity and stability). This gain in spatial coding resolution was more pronounced near the objects and could be rapidly tuned by their manipulations. In addition, place cells displayed improved theta phase precession in the presence of objects. Thus the hippocampal mapping system can dynamically adjust its spatial coding resolution to local sensory cues available in the environment.

Introduction

Animals can flexibly navigate in their environment. In mammals such as rodents and humans, this ability is thought to rely on an internal cognitive map (Epstein et al., 2017; Tolman, 1948). When animals move in their environment, hippocampal place cells fire in specific locations (their place fields) and this spatial tuning is believed to provide a neuronal substrate to the cognitive map (O'Keefe and Dostrovsky, 1971; O'Keefe and Nadel, 1978). To be useful for navigation, such spatial representation should be properly oriented (Marchette et al., 2014) and positioned in reference to the external world. Decades of research have shown that distal visual cues (Muller and Kubie, 1987; O'Keefe, 1976; Shapiro et al., 1997) or intramaze objects located at the border of an environment (Cressant et al., 1997; Renaudineau et al., 2007) play a predominant role in map orientation while environmental boundaries are important for map anchoring (Knierim and Hamilton, 2011; Knierim and Rao, 2003; O' Keefe and Burgess, 1996). Spatial coding resolution could also be important for spatial navigation (Geva-Sagiv et al., 2015). Wild animals, including rodents, often travel kilometers away from their home through empty space to specific food locations (Taylor, 1978). Mapping all traveled space at similar spatial resolution (same density and size of place fields) would require a huge neuronal and computational investment (Geva-Sagiv et al., 2015). On the other hand, mapping different parts of an environment at different spatial resolutions could be ethologically advantageous. Previous studies have reported increased place field density near rewarded locations (Danielson et al., 2016; Dupret et al., 2010; Hollup et al., 2001; O'Keefe and Conway, 1978; Sato et al., 2018), salient cues (Hetherington and Shapiro, 1997; Sato et al., 2018; Wiener et al., 1989) or connecting parts in multi-compartment environments (Spiers et al., 2015). However, whether these overrepresentations correspond to spatial coding at higher resolution or non-spatial coding (e.g., emotional value or specific sensory cues associated with a particular location) is difficult to disentangle. If they would represent increased spatial resolution, then place fields should not only be quantitatively but also qualitatively improved (e.g., spatial selectivity, spatial information content, stability, temporal coding accuracy).

Here we took advantage of virtual reality (Aghajan et al., 2015; Aronov and Tank, 2014; Chen et al., 2013; Cohen et al., 2017; Domnisoru et al., 2013; Harvey et al., 2009; Holscher, 2005; Ravassard et al., 2013; Schmidt-Hieber and Häusser, 2013; Youngstrom and

Strowbridge, 2012) to test this hypothesis, focusing on local visual cues (virtual 3D objects) with higher sensory resolution compared to distal visual landmarks. These could play an important role in setting hippocampal spatial resolution, according to sensory based models of place cell activation (Barry et al., 2006; Geva-Sagiv et al., 2015; Hartley et al., 2000; O' Keefe and Burgess, 1996 ; Sheynikhovich et al., 2009; Strösslin et al., 2005). Virtual reality allows a better control of other local sensory cues (e.g., tactile, olfactory) which even if present are useless for self-location in the virtual reality environment. In this assay, local sensory cues can also be manipulated quickly and reliably without overt changes in context or behavior. We show that sparse local visual cues (3D objects) are sufficient to increase spatial resolution through a higher proportion of place cells, decreased place field size, increased spatial selectivity, spatial information content, stability and temporal coding. Spatial coding resolution was increased locally near objects and could be rapidly tuned upon objects manipulations. Altogether our results suggest that local visual cues could locally and dynamically tune hippocampal spatial coding resolution.

Results

Effects of virtual 3D objects on spatial coding resolution

Head-fixed mice were trained to run on a wheel and to shuttle back and forth on a 2 m-long virtual linear track to collect liquid rewards at its extremities (Fig. 1A). The lateral walls of the virtual track displayed distinct visual patterns to provide directional information. However, these patterns did not provide any information relative to the position of the animal on track. To investigate the contribution of local cues to hippocampal spatial representation, mice were trained either in the presence or absence of 3D Objects (Object Track, OT: n = 2 mice vs No Object Track, ØT: n = 3 mice), which were virtually positioned on the floor of the track between the animal trajectory and the walls (Fig. 1B). The running wheel forced the animals to run in a unidirectional manner so that they repetitively ran along the objects without the possibility to orient toward them or explore them with any sensory modality but vision. Animals received a reward (sucrose in water 5%) each time they reached one of the extremities of the linear track. After licking, the mice were "teleported" in the same position but facing the opposite direction of the track (Fig. 1C), allowing them to run back and forth in the same environment. Once animals reached a stable and proficient behavior (at least 1 reward/minute during a 60 min-long session), we recorded spiking activity in the pyramidal cell layer of the CA1 hippocampal region using either 4-shanks or 8-shanks silicon probes (Fig. 1A) in the right and/or left hemispheres over the course of 2-3 days. A total of 1124 neurons were recorded in the CA1 pyramidal cell layer. Mice trained in ØT (n = 9 recording sessions) performed the task with similar proficiency than mice trained in OT (n = 5 recording sessions), as shown by similar rate of reward collections (ØT: 1.70 ± 0.29 rewards/minute, n = 9 recording sessions in 3 mice; OT: 1.15 ± 0.09 rewards/minute, n = 5 recording sessions in 2 mice; $P = 0.19$, Wilcoxon rank sum test; all values expressed as mean ± SEM) and average running speed (ØT: 14.1 ± 2.12 cm/s, n = 9 recording sessions in 3 mice; OT: 16.8 ± 1.58 cm/s, n = 5 recording sessions in 2 mice; $P = 0.24$, Wilcoxon rank sum test; Fig. 1C).

To examine how local objects impacted spatial representation of the linear track we first compared the number of track-active putative pyramidal cells to assess for overall excitability and the proportion of place cells among them to assess for spatial resolution. The percentage of track active cells was comparable in between the track without and with

objects (ØT: 66.4 ± 5.8%, n = 7 sessions in 3 mice; OT: 52.8 ± 7.8%, n = 5 sessions in 2 mice; P = 0.18, two-tailed unpaired t-test; Fig. 1D). However, while only 19% of track active cells had at least one place field (place cells) in the empty track (n = 48 place cells), 73% of track active cells were place cells when virtual 3D objects were present (n = 103 place cells; $P < 10^{-4}$, two-tailed unpaired t-test; Fig. 1E). In ØT, place fields were relatively sparse in the middle of the track with a large proportion of them aligned either to the beginning or to the end of the track (End-Track fields: 49.3 ± 8.99%, n = 8 sessions in 3 mice; Fig. 2A). In the maze with objects, however, the majority of fields were located in the middle of the track (On-Track fields: 84.3 ± 1.50%; n = 5 sessions in 2 mice; P = 0.015, two-tailed unpaired t-test; Fig. 2A). Altogether these results suggest that 3D objects can increase spatial coding resolution by increasing the proportion of spatially selective cells notably for the central part of the maze. Another factor influencing spatial resolution is place field size. There was a tendency for place field width (calculated on complete fields) to be lower in the track with objects (ØT: 51.5 ± 3.33 cm, n = 15 place fields; OT: 44.6 ± 1.60 cm, n = 95 place fields; P = 0.056, Wilcoxon rank sum test; Fig. 1G), in agreement with a higher spatial coding resolution. Decreased place field width could be due to spatial shrinking of place fields detected on a trial-by-trial basis, could result from decreased inter-trial variability in their position, or both. To decipher among these possibilities, we detected place fields on single trials then calculated their size and averaged them to get a single value for each place field (Cabral et al., 2014). The size of place fields based on single trial detection was not significantly different between the two conditions (ØT: 34.4 ± 1.2 cm, n = 15 place fields; OT: 33.5 ± 0.6 cm, n = 94 place fields; P = 0.28, Wilcoxon rank sum test). On the other hand, the spatial dispersion of single-trial detected place fields was significantly reduced in the presence of 3D objects (ØT: 11.9 ± 0.90 cm, n = 48 place cells; OT: 7.58 ± 0.55 cm, n = 103 place cells; $P < 10^{-4}$, Wilcoxon rank sum test; Fig. 1H). These results suggest that the decreased place field size resulted from decreased inter-trial spatial dispersion. To further assess inter-trial place field stability, independently from place field detection, we calculated a stability index (based on spatial correlations between all pairs of firing rate vectors, see Material and Methods section). This stability index was significantly lower in the track without objects (ØT: 0.12 ± 0.01, n = 48 place cells; OT: 0.34 ± 0.02, n = 103 place cells; $P < 10^{-4}$, Wilcoxon rank sum test; Fig. 1I). Altogether, these results demonstrate that the presence of virtual objects on the

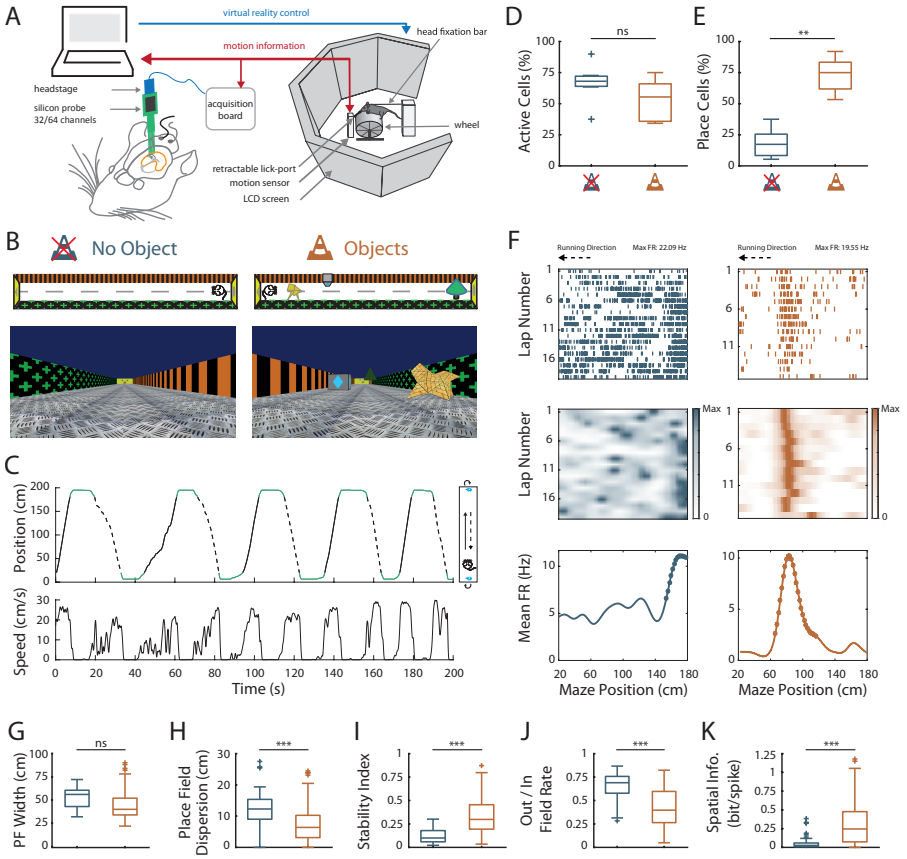

Figure 1: Effects of virtual 3D objects on spatial coding resolution

A. Schema of the virtual reality set up. The mouse is head-fixed and located on a wheel surrounded by LCD screens where a virtual environment is displayed. **B.** Top and first person views of virtual linear tracks used. Left: track without objects (ØT) and right: track with virtual 3D objects (OT). **C.** Top: Animal's position in the virtual track as a function of time. Green lines indicate times when animal was in a reward zone location. These locations were not considered for further analysis. Solid and dotted black lines indicate back and forth trials respectively. Top view of animal in the maze is depicted on the right. Arrows indicate teleportation in the same position but facing opposite direction after reward consumption. Bottom: Animal's speed as a function of time. **D. E.** Box plots of the percentage of active cells (**D**; $P = 0.18$, two-tailed unpaired t-test) and place cells (**E**; $P < 10^{-4}$, two-tailed unpaired t-test) in the maze without (blue) and with (orange) objects (same color code throughout the figures). **F.** Spike raster plots (top) and color-coded firing rate map (middle) for successive trials in one direction (arrow) as a function of the position in the maze. Bottom: corresponding mean firing rate by positions. Dots indicate positions of the detected place field (see Material and Methods). **G-K.** Box plots of the place field width (**G**; $P = 0.056$, Wilcoxon rank sum test), the place field dispersion (**H**; $P < 10^{-4}$, Wilcoxon rank sum test), the stability index (**I**; $P < 10^{-4}$, Wilcoxon rank sum test), the out/in field firing rate (**J**; $P < 10^{-4}$, Wilcoxon rank sum test) and the spatial information (**K**; $P < 10^{-9}$, Wilcoxon rank sum test). For box plots in this and subsequent figures, box extends from the first (Q1) to the third quartile (Q3) with the band inside showing the median and the extremities of the whiskers include values greater than Q1-1.5*(Q3-Q1) and smaller than Q3 + 1.5*(Q3-Q1).

linear track increases spatial coding resolution through an increase in place fields number and a decreased inter-trial spatial dispersion.

To decipher whether objects could qualitatively change place cells' coding resolution we then compared the in-field versus out-of-field firing rates (i.e., signal to noise ratio) of place cells recorded in OT and ØT. In the track without objects, place cells increased their firing rate inside the place field (7.44 ± 0.75 Hz, n = 48 place cells) but also discharged at high rate outside the field (5.23 ± 0.62 Hz; Fig. 1F and J; ratio: 0.65 ± 0.02) indicating a low spatial resolution. In comparison, place cells recorded in the track with objects had comparable firing rates inside the place field (6.73 ± 0.61 Hz, n = 103 place cells; $P = 0.09$, Wilcoxon rank sum test) but fired significantly less outside the field (3.53 ± 0.49 Hz; Ratio: 0.42 ± 0.02; Fig. 1F and J; $P < 10^{-4}$, Wilcoxon rank sum test) indicating increased spatial resolution. Accordingly, spatial information (in bit/spike), a measure independent of place fields' detection (Skaggs et al., 1996) was very low in the track without object (0.06 ± 0.01 bit/spike, n = 48 place cells) and significantly higher in the presence of objects (0.32 ± 0.03 bit/spike, n = 103 place cells; $P < 10^{-9}$, Wilcoxon rank sum test; Fig. 1K). We conclude that local visual cues both quantitatively and qualitatively increase spatial coding resolution.

Virtual 3D objects improve spatial resolution locally

We then wondered whether 3D objects could influence spatial representation locally around the objects. To address this question we focused our analysis on recordings performed in the OT. We first noticed that the distribution of place fields was non-uniform on the track ($P = 0.001$, test of non-uniformity). To quantify more precisely this effect, we divided the linear track in Objects Zones (OZ) and No Objects Zones (ØZ), depending if a given track zone contained an object or not, respectively (Fig. 2A, right). The density of place fields was significantly higher in OZ (OZ: 8.80 ± 1.09% /10 cm, n = 12 spatial bins of 10 cm, 6 in each direction; ØZ: 3.17 ± 0.70% /10 cm, n = 20 spatial bins of 10 cm, 10 in each direction; $P < 10^{-4}$ two-tailed unpaired *t*-test; Fig. 2B and D). Furthermore, in the maze with objects, place fields were significantly smaller in OZ (OZ: 38.4 ± 1.46 cm, n = 50 fields; ØZ: 51.6 ± 2.62 cm, n = 45 fields; $P = 0.00020$, Wilcoxon rank sum test; Fig. 2E). Accordingly, place field dispersion was also significantly reduced in OZ (OZ: 7.15 ± 0.59 cm, n = 87 fields; ØZ: 10.0 ± 0.99 cm, n = 49 fields, $P = 0.011$, Wilcoxon rank sum test). Finally, a local stability index (see Material and Methods section) was significantly increased in OZ (OZ: 0.56 ± 0.02, n = 60 bins

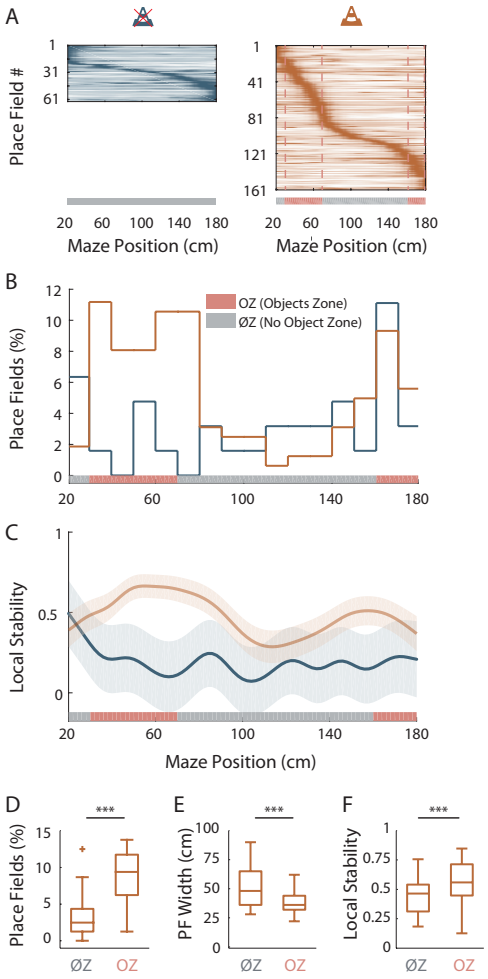

Figure 2: Virtual 3D objects improve spatial resolution locally

A. Color-coded mean firing rate maps of all place fields recorded in the maze without objects (left) or with objects (right). The color codes for the intensity of the bin's mean firing rate normalized on the maximal mean firing rate (peak rate) in the recording session. The place cells are ordered according to the position of their peak rate in the track (reward zones excluded). Bottom: The tracks were divided into Objects Zones (OZ, in red on the x-axis) around the objects and No Object Zones (ØZ, in grey on the x-axis) deprived of objects. Red dotted lines depicts the boundaries of the OZ in the track with objects. **B.** Percentage of On-Track place fields at each spatial bin (10 cm) in the maze with (orange line) and without objects (blue line). **C.** Mean local stability index (solid lines) ± SEM (shaded bands) for place cells with On-Track fields at each spatial bin in the track with (orange) or without (blue) objects. **D-F.** Box plots depicting the mean percentage of place fields per spatial bin (**D**; $P < 10^{-4}$, Wilcoxon rank sum test), the place field width (**E**; $P = 0.00020$, Wilcoxon rank sum test) and the local stability index (**F**; $P < 10^{-4}$, Wilcoxon rank sum test) in OZ and ØZ in the maze with objects.

of 2 cm, 30 in each direction; ØZ: 0.44 ± 0.01, n = 100 bins of 2 cm, 50 in each direction; $P < 10^{-4}$, Wilcoxon rank sum test; Fig. 2C and F). We conclude that 3D objects can locally increase spatial resolution within the same environment.

Finally we found no significant difference in the out-of-field versus in-field firing ratio between fields located in OZ and ØZ (OZ: 0.45 ± 0.03, n = 87 fields; ØZ: 0.41 ± 0.03, n = 49 fields; $P = 0.53$, Wilcoxon rank sum test) nor changes in spatial information (OZ: 0.36 ± 0.04 bit/spike; ØZ: 0.28 ± 0.04 bit/spike; $P = 0.50$, Wilcoxon rank sum test). We conclude that 3D objects can locally increase spatial resolution by a local increase in place field number, a local reduction in place field size and an increased local stability while their effect on spatial information content are global.

Virtual 3D objects improve hippocampal population coding accuracy

The results so far suggest that objects can increase the resolution of hippocampal spatial representation. To verify this we next performed position-decoding analysis (Brown et al., 1998; Pfeiffer and Foster, 2013; Zhang et al., 1998) (Fig. 3A). We used the spike trains from all the pyramidal cells recorded on the track (i.e., both the spatially modulated and non-spatially modulated cells) and compared decoded positions with actual positions of the animal in the virtual linear tracks. Overall, the effect of objects on hippocampal spatial coding was obvious because the decoding error across trials was nearly two fold larger in the track without objects compared to the track with objects (ØT: 46.3 ± 0.05 cm, n = 180 trials; OT: 27.6 ± 0.12 cm, n = 129 trials; $P < 10^{-23}$, Wilcoxon rank sum test; Fig. 3A and B). Accordingly, the decoding accuracy (van der Meer et al., 2010) was three fold lower in the empty track compared to the track with objects (ØT: 0.017 ± 2.8 X 10^{-5}, n = 180 trials; OT: 0.053 ± 2.06 x 10^{-4}, n = 129 trials; chance level 0.01; $P < 10^{-41}$, two-tailed unpaired *t*-test; Fig. 3A and C). In both cases, downsampling was performed to equalize the number of cells used for decoding between the two conditions (20 active cells). These effects were independent of the decoding method used because similar results were observed using a Firing Rate Vector (FRV) method (Middleton and McHugh, 2016; Wilson and McNaughton, 1993). Correlation values were lower in the empty track (ØT: 0.63 ± 0.008, n = 180 trials; OT: 0.74 ± 0.01, n = 129 trials; $P < 10^{-17}$, Wilcoxon rank sum test) and decoding errors were higher (ØT: 48.4 ± 0.67 cm, n = 180 trials; OT: 33.0 ± 1.81 cm, n = 129 trials; $P < 10^{-12}$, Wilcoxon rank sum test). Because Bayesian decoding was performed using a drop cell approach we could

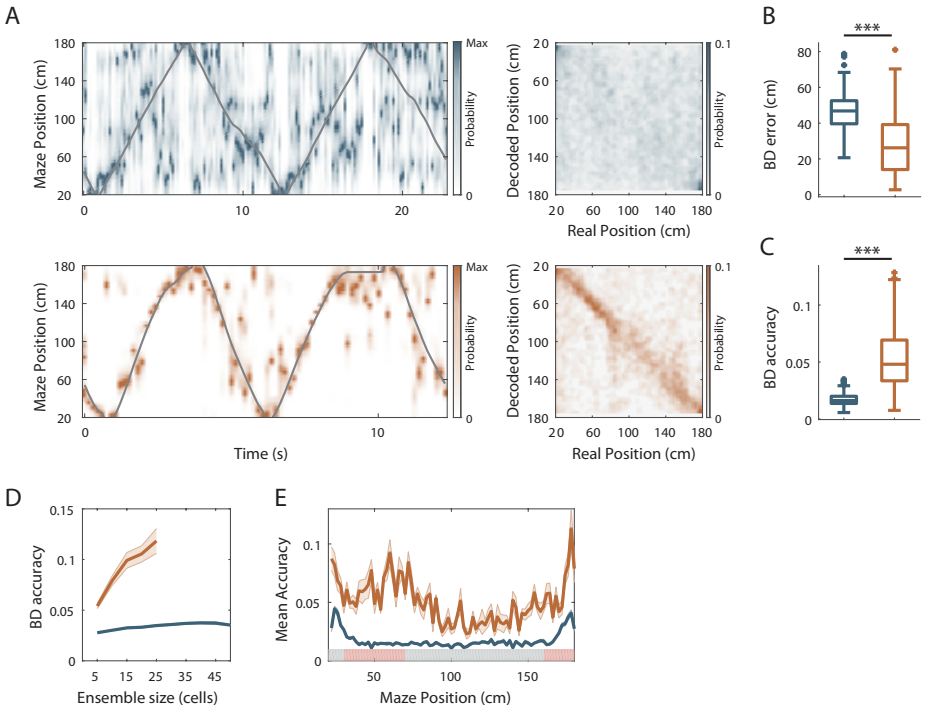

Figure 3: Virtual 3D objects improve hippocampal population coding accuracy

A. Left: Color-coded distribution of the animal position's probability in the virtual track (the reward zones are excluded) computed using a Bayesian decoder (see Material and Methods) at each time window (500 ms) illustrated during 4 trials in the maze without (top) and with (bottom) objects. Spike trains of active cells were used to compute the animal position's probability. For visualization purpose, position probability is normalized by its maximum at each time bin. The real position is indicated with a solid grey line. Right: Confusion matrix between the real (x-axis) and the decoded position (y-axis) for all recording sessions performed on the track without objects (top) or with objects (bottom). **B.** Box plots depicting the Bayesian decoding error (BD error) in the maze with and without objects. The BD error was significantly higher in the maze deprived of objects ($P < 10^{-23}$, Wilcoxon rank sum test). **C.** Box plots depicting the Bayesian decoding accuracy (BD accuracy) in the maze with and without objects. The BD accuracy was significantly higher in the maze with objects ($P < 10^{-41}$, two-tailed unpaired t-test). **D.** Mean BD accuracy (solid lines) ± SEM (shaded bands) as a function of a subset of active cells in the maze with and without objects. **E.** Mean BD accuracy (solid lines) ± SEM (shaded bands) at each position in the maze with and without objects. The track was divided in two zones: Objects Zone (OZ, in red on the x axis) around the objects and No Object Zone (ØZ, in grey on the x axis) deprived of objects. Note that the decoding accuracy was specifically improved in OZ in comparison to ØZ in the maze with objects ($P < 10^{-6}$, Wilcoxon rank sum test).

185 measure decoding accuracy for different sample sizes of active cells (van der Meer et al.,
186 2010) (Fig. 3D). Decoding accuracy was positively correlated with sample size in the track
187 with objects but not in the track without objects (Fig. 3D). Importantly, in the track without
188 objects, the decoding accuracy never reached values observed for the track with objects,
189 even when using a larger set of cells (up to 45). To see if objects could locally increase spatial
190 decoding accuracy we compared decoding accuracy between OZ and ØZ. While decoding
191 accuracy was uniformly low in the track without objects (OZ: 0.019 ± 0.0014, n = 30 spatial
192 bins of 2 cm; ØZ: 0.016 ± 9.25 x 10^{-4}, n = 50 spatial bins of 2 cm; P = 0.17, Wilcoxon rank sum
193 test; Fig. 3E), it was increased in every part of the track with objects but significantly more in
194 OZ compared to ØZ (OZ: 0.061 ± 0.002, n = 30 spatial bins of 2 cm; ØZ: 0.043 ± 0.002, n = 50
195 spatial bins of 2 cm; $P < 10^{-6}$, Wilcoxon rank sum test; Fig. 3E). We concluded that local visual
196 cues can globally and locally improve spatial coding accuracy at the population level.
197

198 **Effects of online object manipulation**

199 Place cells usually appear instantaneously upon exploration of a new environment in area
200 CA1 (Wilson and McNaughton, 1993). To see if similar dynamics could be observed for the
201 effects of virtual objects on spatial resolution we manipulated objects online while recording
202 the same ensemble of cells in area CA1. For mice trained in an empty track, we
203 instantaneously added the three objects (which were thus new to the mice) after 20 min of
204 recordings. Conversely, for mice trained in the track with objects we instantaneously
205 removed the three objects. Objects manipulation had no effect on the proportion of active
206 cells (Fig. 4B) but a strong impact on the proportion of place cells (Fig. 4A and C). For mice
207 trained in an empty track, adding objects instantaneously increased the proportion of place
208 cells (from 21.6 ± 5.3% to 75.0 ± 4.0%; n = 5 sessions in 3 mice; $P < 10^{-5}$, two-tailed paired t-
209 test; Fig. 4A and C). Thus, a large proportion of cells initially silent or active but non-spatially
210 modulated in the familiar empty track became spatially modulated (36.3%). Some cells
211 initially spatially modulated remained place cells (7.4%) while others became non-spatially
212 modulated or silent (2.4%). Most of the new place cells had on-track fields (81.3%; Fig. 4H).
213 Adding objects also increased place cells' spatial information (P = 0.001, Wilcoxon rank sum
214 test; Fig. 4E) and stability ($P < 10^{-5}$, Wilcoxon rank sum test; Fig. 4G). The increase in stability
215 was specifically observed in OZ (Fig. 4I; $ØT_{fam}$ vs OT_{new} for OZ: $P < 10^{-6}$, Wilcoxon rank sum
216 test; for ØZ: P = 0.15, Wilcoxon rank sum test). Place fields' out/in field firing ratio and

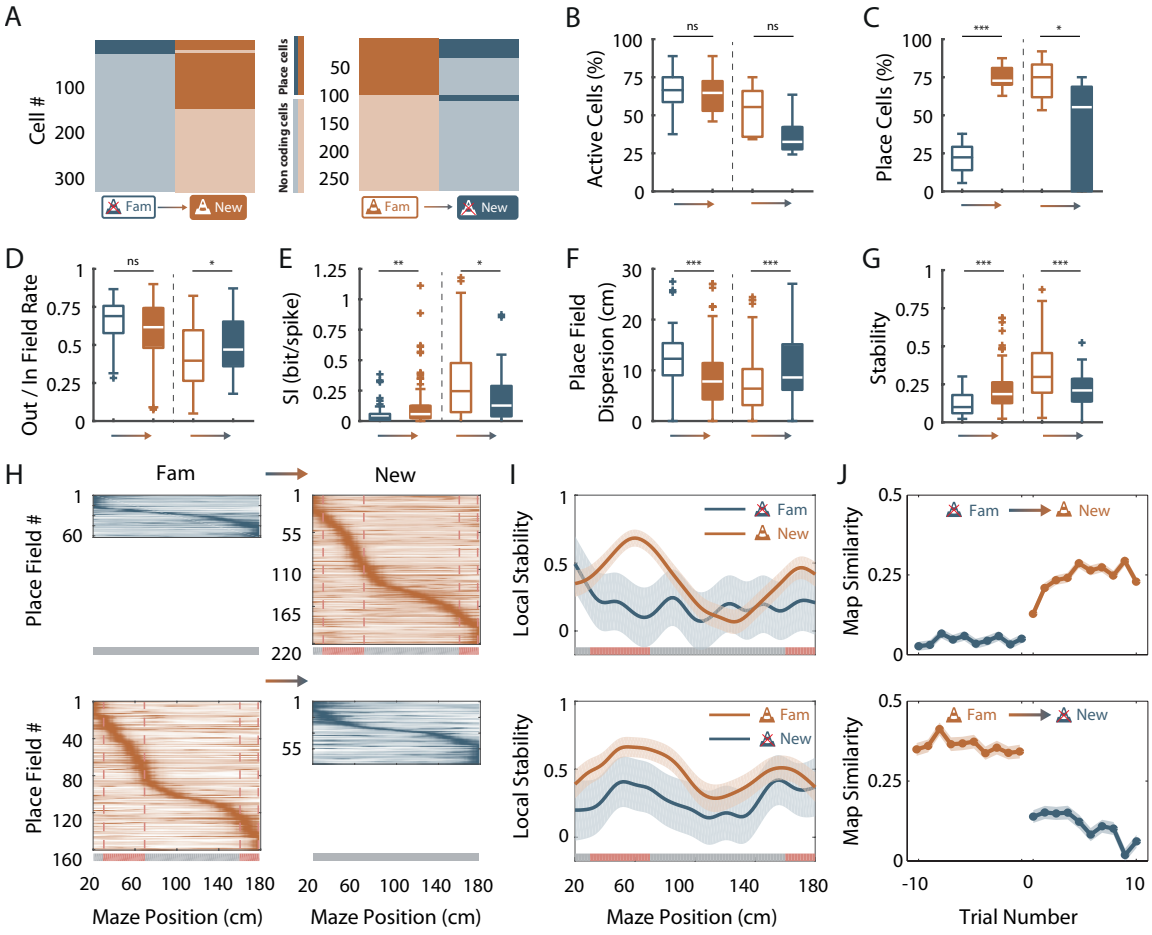

Figure 4: Effects of online object manipulation

A. Mosaic plots representing the cells classified as place cells (darker orange and blue) or non-coding cells (i.e. silent or active non-coding, lighter orange and blue) in the familiar and the new mazes. **B-G.** Box plots comparing familiar (empty box) and new mazes (filled box) conditions. Two pairs of box plots are illustrated; Left: comparison between the familiar maze without objects (blue, $ØT_{fam}$) and the new maze with objects (orange, OT_{new}). Right: comparison between the familiar maze with objects (orange, OT_{fam}) and the new maze without objects (blue, $ØT_{new}$). A gradient color arrow shows the way of the transition. Plots show the percentage of active cells (**B;** $ØT_{fam}$ vs OT_{new}: $P = 0.66$; OT_{fam} vs $ØT_{new}$: $P = 0.14$, two-tailed paired t-test), the percentage of place cells (**C;** $P < 10^{-5}$ and $P = 0.04$, respectively, two-tailed paired t-test), the Out/In field firing rate (**D;** $P = 0.06$ and $P = 0.047$, respectively, Wilcoxon rank sum test), the spatial information (SI; **E**; $P = 0.001$ and $P = 0.015$, respectively, Wilcoxon rank sum test), the place field dispersion (**F;** $P < 0.0004$ and $P = 0.0009$, respectively, Wilcoxon rank sum test) and the stability index (**G;** $P < 10^{-5}$ and $P = 0.0002$, respectively, Wilcoxon rank sum test). **H.** Color-coded mean firing rate maps of place fields recorded in the familiar and new mazes. The color codes for the intensity of the firing rate normalized by the peak rate. The place fields are ordered according to the position of their peak rate in each track (the reward zones are excluded). The tracks were divided into Objects Zones (OZ, in red on the x-axis) around the objects and No Object Zones (ØZ, in grey on the x-axis) deprived of objects. Red dotted lines depicts the boundaries of the OZ in the track with objects. **I.** Mean local stability index (solid orange or blue lines) ± SEM (blue or orange shaded areas) at each spatial bin in the familiar and new mazes (top: from $ØT_{fam}$ to OT_{new}; bottom: from OT_{fam} to $ØT_{new}$). **J.** Map similarity (see Material and Methods) for 10 trials before and 10 trials after the experimental manipulation (indicated by 0) for $ØT_{fam}$ to OT_{new} (top) and for OT_{fam} to $ØT_{new}$ condition (bottom).

dispersion were instantaneously decreased ($P < 0.0004$ and $P = 0.06$, respectively, Wilcoxon rank sum test; Fig. 4D and F). On the other hand, removing objects decreased the proportion of place cells (from 73.1 ± 6.62% to 39.4 ± 16.4%, n = 5 sessions in 2 mice; $P = 0.04$, two-tailed paired *t*-test; Fig. 4 A and C). The spatial information and stability were decreased by this manipulation ($P = 0.015$ and $P = 0.0002$, respectively, Wilcoxon rank sum test; Fig. 4E and G) while place field out/in field firing ratio and dispersion were increased ($P = 0.0009$ and $P = 0.047$, respectively, Wilcoxon rank sum test; Fig. 4D and F). The effect on stability was global rather than local (Fig. 4I; OZ: $P < 10^{-10}$, two-tailed unpaired *t*-test; ØZ: $P < 10^{-13}$, Wilcoxon rank sum test). We conclude that the effects of virtual 3D objects on place cells coding observed between familiar tracks can be reproduced with instantaneous objects manipulation.

To get a better idea of the dynamic of these changes we correlated the firing rate maps of each back and forth trial with the corresponding average firing rate map in the condition with objects (the most stable condition) for 10 trials before (t-1 to t-10) and 10 trials after (t+1 to t+10) the manipulation (Fig. 4J). When objects were added in the empty track, map similarity was significantly higher for the second trial in the new condition (t-1 vs t+1, n = 598 pyramidal cells; $P = 0.058$, Kruskall-Wallis one-way test; t+1 vs t+2, n = 614 pyramidal cells; $P = 0.029$, Kruskall-Wallis one-way test) and then stayed higher from this second trial on (t+2 vs t+3, n = 608 pyramidal cells; $P = 0.99$, Kruskall-Wallis one-way test). Conversely, when objects were removed from the familiar track with objects, map similarity dropped already for the first trial in the new condition (t-1 vs t+1, n = 380 pyramidal cells; $P < 10^{-6}$, Kruskall-Wallis one-way test) and stayed lower from this first trial on (t+1 vs t+2, n = 380 pyramidal cells; $P = 1$, Kruskall-Wallis one-way test). Thus, the hippocampus can rapidly adapt its spatial coding resolution to local visual cues available in the environment.

Effects of virtual 3D objects in a visually enriched environment

We next wondered whether the hippocampal mapping resolution was maximal in the presence of objects or whether it could be further increased by visually enriching the environment. We thus analyzed hippocampal place cells' coding in another environment containing the original 3D objects but enriched in visual cues such as wall patterns in different positions along the track and high 3D columns outside the track (EOT, n = 3 mice; Fig. 5A). The percentage of active cells was not increased by visually enriching the

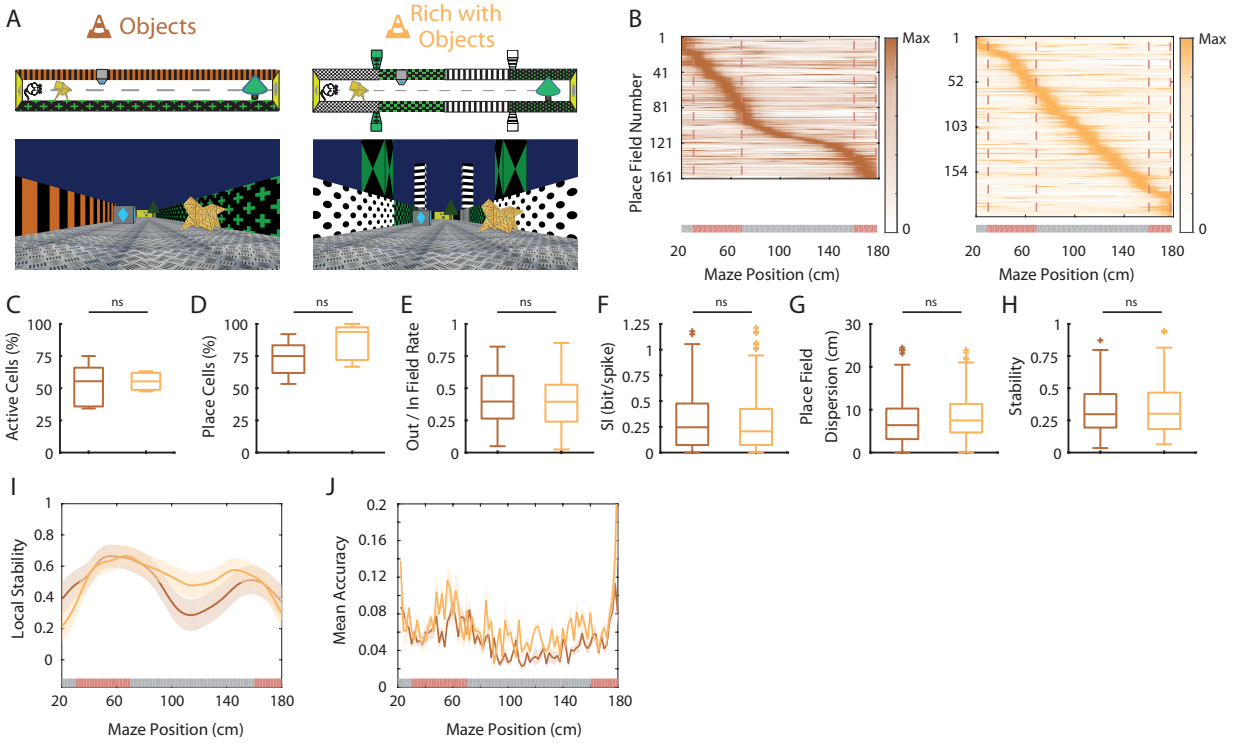

Figure 5: Effects of virtual 3D objects in a visually enriched environment

A. Schema (top) and picture (bottom) representing the original maze with objects (left) and a visually enriched maze with objects (right). **B.** Color-coded mean firing rate maps for all place fields recorded in the original maze with objects (orange, left) and on the visually rich maze with objects (yellow, right). The color codes for the intensity of the firing rate normalized by the peak rate. The place fields are ordered according to the position of their peak rate in each track (the reward zones are excluded). The tracks were divided into Objects Zones (OZ, in red on the x-axis) around the objects and No Object Zones (ØZ, in grey on the x-axis) deprived of objects. Red dotted lines depicts the boundaries of the OZ. **C-H.** Box plots representing in the original (orange) and visually rich (yellow) maze with objects the percentage of active cells (**C;** $P = 0.77$, two-tailed unpaired t-test), the percentage of place cells (**D;** $P = 0.20$, two-tailed unpaired t-test), the out/in field rate (**E;** $P = 0.57$, Wilcoxon rank sum test), the spatial information (SI; **F;** $P = 0.67$, Wilcoxon rank sum test), the place field dispersion (**G;** $P = 0.06$, Wilcoxon rank sum test) and the stability index (**H;** $P = 0.95$, Wilcoxon rank sum test). **I.** Mean local stability index (solid orange or yellow lines) ± SEM (orange or yellow shaded bands) at each position's bin in the original (orange) and visually rich (yellow) mazes. **J.** Mean BD accuracy (solid lines) ± SEM (shaded bands) at each spatial bin in the original maze with objects (orange) or in the visually rich maze with objects (yellow).

environment (OT, n = 5 sessions in 2 mice; EOT, n = 5 sessions in 3 mice; $P = 0.77$, two-tailed unpaired *t*-test) nor was the percentage of place cells (OT, n = 5 sessions in 2 mice; EOT, n = 5 sessions in 3 mice; $P = 0.20$, two-tailed unpaired *t*-test; Fig. 5B-D). However, place fields were uniformly distributed along the track in the visually rich environment (n = 16 spatial bins of 10 cm; $P = 0.23$, test for non-uniformity), thus not clustered around objects as in the visually poor environment (Fig. 5B). This suggests that local visual cues are important to set place field position (Renaudineau et al., 2007). However, all other attributes of place fields were not significantly different between the two environments (OT, n = 103 place cells; EOT, n = 132 place cells; Out-field/In-field firing rates: $P = 0.57$; Spatial info: $P = 0.67$; Dispersion: $P = 0.06$; Stability: $P = 0.95$; Wilcoxon rank sum test for all; Fig. 5E-H). When looking at local stability of firing rates, we still observed a significant effect of objects in the visually enriched environment in OZ versus ØZ (OZ, n = 60 spatial bins of 2 cm; ØZ: n = 100 spatial bins of 2 cm; $P = 0.014$, Wilcoxon rank sum test; Fig. 5I). Interestingly, positions near objects were also decoded with a better accuracy using a Bayesian decoder than positions further away in the visually enriched environment (OZ: 0.08 ± 0.007, n = 30 spatial bins of 2 cm; ØZ: 0.059 ± 0.002, n = 50 spatial bins of 2 cm; $P = 0.002$, Wilcoxon rank sum test; Fig. 5J). Altogether these results suggest that in the presence of local visual cues, hippocampal spatial coding is not further improved by visually enriching the environment. However, place fields locations are influenced by additional visual cues along the track. Interestingly, despite a homogenous distribution of place field locations, 3D objects could still locally influence hippocampal population decoding accuracy.

Virtual 3D objects improve temporal coding

The results so far suggest that local 3D objects can increase spatial coding resolution when considering the spatial firing rate code. Place cells however do not only increase their firing rate inside the place field but also tend to fire at progressively earlier phases of the theta oscillation as an animal moves through the place field (O'Keefe and Recce, 1993). This phenomenon, called theta phase precession, is thought to further increase spatial coding resolution because different locations within the place field that are difficult to distinguish based on firing rate alone can be accurately separated when phase is taken into account. In the temporal domain, increased spatial resolution would thus correspond to increased slope of the phase versus position relationship.

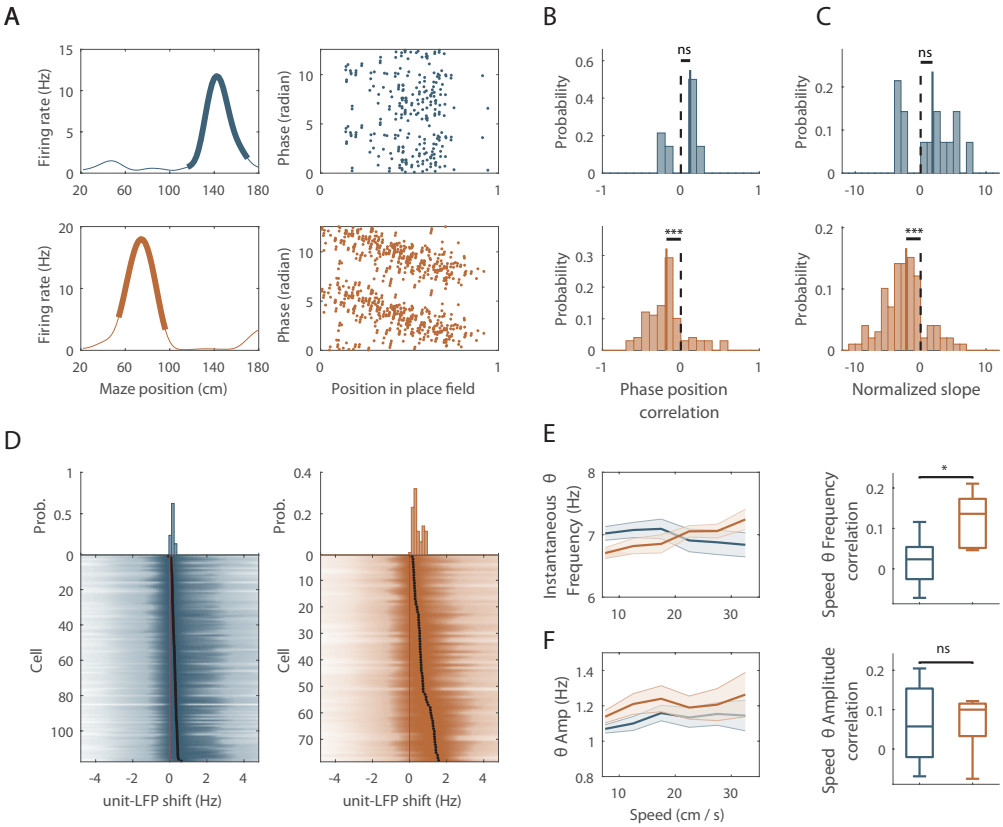

Figure 6: Virtual 3D objects improve temporal coding

A. Left: Mean firing rate maps of representative CA1 place cells with place fields highlighted by a bold line (left) recorded in the maze without objects (top, only spatially stable trials see Material and Methods section) and with objects (bottom). Right: spikes phase (radian) versus position in the corresponding place fields. **B-C.** Distribution of significant phase position correlation (**B**) and slopes (**C**) in the condition without objects (top; correlation: $P = 0.42$; slopes: $P = 0.4$, one-sample sign-test) and with objects (bottom; correlation: $P < 10^{-11}$; slopes: $P < 10^{-11}$, one-sample sign-test). The median of the distribution is indicated by a bold line and 0 by a dotted line. **D.** Color-coded cross-correlogram between the power spectra of neuronal spikes and LFP for each theta-modulated cell recorded on the maze without (bottom left, blue) and with (bottom right, orange) objects. Black dots indicate the maximum of each cross-correlation. Each cross-correlation is normalized by its maximum. Top: Distribution of the maximum cross-correlations used to quantify the frequency shift for all the cells. **E-F.** Instantaneous LFP theta frequency (**E**) and amplitude (**F**) as a function of the animal's speed in the track with or without objects. Left: Mean theta frequency (**E**) or amplitude (**F**) across all recording sessions each 5 cm/s bin. Right: Box plots of the correlation between theta frequency (**E**; $P = 0.01$, two-tailed unpaired t-test) or amplitude (**F**; $P = 0.9$, two-tailed unpaired t-test) vs speed for individual sessions.

We first looked for differences in the theta oscillation recorded in the Local Field Potential (LFP) between the two conditions. The mean frequency of the field theta oscillation was not significantly different when mice were running in the track with or without objects (ØT: 6.79 ± 0.12 Hz, n = 9 sessions in 3 mice; OT: 6.77 ± 0.10 Hz, n = 5 sessions in 2 mice; $P = 0.28$, Wilcoxon rank sum test) but was lower than that reported for mice navigating in real linear tracks (Middleton and McHugh, 2016), as observed for rats navigating virtual linear tracks (Ravassard et al., 2013). The power of theta oscillation (theta index see Material and Methods section) was also not significantly different (ØT: 3.22 ± 0.23, n = 9 sessions in 3 mice; OT: 3.59 ± 0.22 Hz, n = 5 sessions in 2 mice; $P = 0.28$, two-tailed unpaired *t*-test). Theta frequency was not modulated by running speed of the animal in ØT (r = 0.02 ± 0.02, n = 9 sessions in 3 mice; Fig. 6E) as previously observed in virtual linear tracks when only distal cues are present (Ravassard et al., 2013). This modulation was however significant in OT (r = 0.14 ± 0.03, n = 5 sessions in 2 mice; $P = 0.01$, two-tailed unpaired *t*-test; Fig. 6E). In contrast, theta amplitude was similarly modulated by running speed in both conditions (ØT: r = 0.06 ± 0.03, n = 9 sessions in 3 mice; OT: r = 0.1 ± 0.04, n = 5 sessions in 2 mice; $P = 0.9$, two-tailed unpaired *t*-test; Fig. 6F).

We then analyzed place cells' theta phase precession. To compensate for decreased spatial stability in the ØT conditions we took into account only trials with good correlation with the average place fields (Spatially Stable Trials or SST) for place cells recorded in the empty track (Schlesiger et al., 2015), but included all trials for place cells recorded in the track with objects. The stability index of SST fields in ØT was not significantly different from the stability index of all fields in OT (ØT, n = 62 SST fields; OT, n = 198 fields; $P = 0.8$, Wilcoxon rank sum test). The percentage of fields with significant ($P < 0.05$) and negative correlation between phase and position (i.e., precessing fields) was high in the track with objects (41.9%), comparable to that observed in real linear tracks in mice but low in the empty track (8%; $P < 10^{-4}$ compared to OT, Chi-Square test). Accordingly, the correlation between phase and position was significantly different from zero for place cells recorded in the track with objects (r = -0.18 ± 0.018, n = 99 fields; $P < 10^{-11}$, sign-test; Fig. 6A and B) but not for those recorded in the track without objects (r = 0.03 ± 0.026, n = 14 fields; $P = 0.42$, sign-test; Fig. 6A and B). Moreover, phase precession slopes (calculated on normalized place field sizes) were negative and significantly different from 0 for cells recorded in the track

with objects (-2.43 ± 0.23 rad/U, n = 99 fields; $P < 10^{-11}$, sign-test; Fig. 6C) but not in the track without objects (1.18± 0.50 rad/U, n = 14 fields; $P = 0.4$, sign-test; Fig. 6C).

In the track without objects, the decrease in phase-position correlation could result from the higher inter-trial spatial dispersion which could lead to spikes at different theta phases for identical positions (Mizuseki et al., 2009; Schlesiger et al., 2015). To assess this possibility, we performed phase-precession analysis on single-trial-detected fields and averaged the slopes of individual passes (Schlesiger et al., 2015; Schmidt et al., 2009). The correlation was still negative and significantly different from 0 in OT (r = -0.19 ± 0.29, n = 198 single-trial fields; $P < 10^{-4}$, one-sample *t*-test) but not in ØT (r = -0.004 ± 0.03, n = 62 single-trial fields; $P = 0.92$, one sample *t*-test). Similarly, the slope of the regression line was negative and significantly different from 0 in OT (-2.27 ± 0.56 rad/U, n = 198 single-trial fields; $P = 0.004$, sign-test) but not in ØT (0.79 ± 0.56, n = 62 single-trial fields; $P = 0.73$, sign-test).

Because a low percentage of active cells were place cells in the track without objects, we performed an additional analysis that is independent of place field detection. It exploits the fact that a phase precessing cells emit theta paced spikes at a frequency slightly faster than the concurrent LFP theta oscillation (O'Keefe and Recce, 1993). We performed cross-correlation between the power spectra of neuronal spikes and LFP for all active cells with significant theta modulation of spiking activity (ØT: 117/342 cells = 34.2%; OT: 78/142 cells = 54.9%; $P <10^{-4}$, Chi-square test) and compared the frequency shift (>0) between spiking and LFP theta oscillations between the two conditions (Geisler et al., 2007) (Fig. 6D). The shift was significantly higher in the OT (0.72 ± 0.05 Hz, n = 78 active cells. Fig. 6D) versus ØT (0.26 ± 0.01 Hz, n = 117 active cells; $P < 10^{-17}$, Wilcoxon rank sum test; Fig. 6D). Altogether, these results suggest that phase precession is increased in the presence of intramaze local visual cues.

Discussion

Spatial resolution can be improved by pooling information across neurons (Wilson and McNaughton, 1993). We found that local visual cues could dramatically increase the number of place cells among active cells (by a 3 fold factor). The mechanisms of place cell activation are not fully understood. Using sensory-based models of place cells activation (Barry et al., 2006; Hartley et al., 2000; Sheynikhovich et al., 2009; Strösslin et al., 2005) one can predict that increasing the quantity/quality of sensory cues in an environment will increase the number of place cells coding that environment (Geva-Sagiv et al., 2015). However, studies so far have revealed an homogeneous allocation of place fields in space (Muller et al., 1987; Rich et al., 2014) in a given environment and examples of over representations were difficult to disentangle from the coding of non spatial information such as the emotional value (Danielson et al., 2016; Dupret et al., 2010; Hollup et al., 2001; O'Keefe and Conway, 1978; Sato et al., 2018) or specific distal sensory cues (Hetherington and Shapiro, 1997; Sato et al., 2018; Wiener et al., 1989) associated with a particular location. Previous studies using local enrichment with multimodal sensory cues yield contrasting results. One study recording in the dorsal hippocampus in rats navigating between cue rich and cue poor parts of the same track reported no effect on the number of place cells activated or on the density of place fields. Population vector analysis nevertheless revealed increased disambiguation of nearby locations in the cue rich condition suggesting increased spatial resolution (Battaglia, 2004). Others studies found no overall increase of place cells proportion in 2D environment containing objects nor a specific bias for place cells to fire near the objects (Deshmukh and Knierim, 2013; Renaudineau et al., 2007). One possibility to explain the lack of recruitment of additional cells in these studies could be a high recruitment rate of the dorsal hippocampus even in the "cue poor" condition due to the availability of distal visual cues or the presence of uncontrolled local cues (Ravassard et al., 2013). Another study tested this hypothesis by recording in the intermediate/distal hippocampus, which has a lower rate of spatially modulated cells and is more heavily innervated by the lateral entorhinal cortex where object responsive cells have been recorded (Deshmukh and Knierim, 2011). In this study, an increase number of place cells were recorded when real 3D objects were present on the track compared to an empty track (Burke et al., 2011). However, the effect was smaller than the one reported here and the number of CA1 pyramidal cells activated at any

given spatial location was not significantly different between the tracks with and without objects. In our study, however, the number of CA1 pyramidal cells activated at a given location was significantly increased (see Fig. 2), specifically for locations near objects.

Newly activated place cells could correspond to landmark vector (LV) cells, which have been recorded in the hippocampus of freely moving rats (Deshmukh and Knierim, 2013) and head-fixed mice running on a treadmill (Geiller et al., 2017). These cells tend to discharge systematically near objects present in the environment or landmarks on the treadmill. To test this hypothesis we specifically looked for LV cells in our recordings. On individual trials the presence of LV cells firing near a specific object was difficult to disentangle from the firing of a place cell which happened to have a place field near that object. We thus used back and forth trials to dissociate these possibilities. We defined object zones for each individual object (IOZ, which were enlarged on the side from which animals were approaching the object to take into account the anticipatory nature of some LV cells (Geiller et al., 2017). We classified place cells as LV cells if they were bidirectional and had at least one place field in an IOZ corresponding to the same object for back and forth trials. In the track without objects no LV cells were detected. In the track with objects, LV represented only 6.79 % of all place cells. Thus a large proportion of newly activated place cells in the presence of objects are not LV cells. The low number of LV cells in our recordings was comparable to that of a previous study with real 3D objects in a 2D environment (Deshmukh and Knierim, 2013) but lower than that observed in a treadmill with tactile cues (Geiller et al., 2017). This could result from the fact that our local visual stimuli provided a less overwhelming sensory stimulation than tactile cues used on the treadmill (Geiller et al., 2017). Nevertheless, our local visual stimuli could still substantially increase the number of place cells coding that environment.

A previous study specifically tested the role of distal visual cues in place cell activation using virtual reality environments in rats (Ravassard et al., 2013). They reported a lower number of active cells in the virtual environment and concluded that distal visual cues alone are not sufficient to fully engage the hippocampal mapping system. Our results complement this study by showing that local visual cues can increase the number of spatially selective cells. Our results are also consistent with local visual cues being used by the system to increase qualitatively spatial coding. Spatial selectivity was increased in the presence of objects by specifically decreasing out-of-field firing rate. A plausible mechanism for this

400 increased selectivity would be an increase in interneurons activity. Interneuron inhibition
401 using optogenetic tools increases out-of-field firing thus reducing spatial selectivity
402 (Grienberger et al., 2017). Inter-trial stability of place fields was also specifically increased in
403 the maze with objects and a Bayesian decoder performed better in the presence of objects.
404 Thus the hippocampus is not only quantitatively but also qualitatively more engaged in
405 spatial coding in the presence of objects. Most studies in real environments focused on the
406 role of visual cues in place fields orientation or location (Knierim and Hamilton, 2011) but did
407 not specifically addressed the influence of local cues on place cells' coding quality. Previous
408 work comparing real and virtual environment failed to reveal an effect of distal visual cues
409 on spatial coding specificity (Ravassard et al., 2013). Several factors could explain the specific
410 effects of local visual cues on spatial selectivity and stability. First, objects could constitute a
411 stable reference point in space to refine estimation of the current subject's position possibly
412 through anchoring of the path integrator system (McNaughton et al., 2006; Poucet et al.,
413 2015). Close to the objects, this effect could be further increased through motion parallax
414 effect. Second, objects could increase the resolution of visual cues available to the animal
415 notably compared to distal cues which. An increase in sensory resolution can be converted
416 to increased spatial coding resolution according to sensory based models of place cell
417 activation (Barry et al., 2006; Hartley et al., 2000; Strösslin et al., 2005). Third, objects as
418 salient cues in the environment could increase the attentional state of the animal and favor
419 spatial awareness. Such increase in attention has been shown to increase spatial selectivity
420 in mice (Kentros et al., 2004) as well as sensory coding (McGinley et al., 2015). However, we
421 note that animals were not required to pay close attention to objects locations to perform
422 the task and task performance was not different between the ØT and OT conditions.
423 Alternatively, objects could represent a source of additional noise in the system thus
424 requiring a higher number of spatially modulated cells and increased spatial selectivity for
425 efficient position coding. However, position decoding was very poor in the maze without
426 objects, which argues against this possibility.

427 The effects of local cues on spatial coding accuracy were even more pronounced in
428 the temporal domain. Indeed, in the absence of local cues theta phase precession was
429 strongly reduced as observed in rat running in place on a wheel (Hirase et al., 1999) despite
430 the presence of place fields. When local cues were included, however, hippocampal place
431 cells precessed at a rate comparable to that observed in real environments (Middleton and

McHugh, 2016). To ascertain that this effect did not result from changes in place fields' quality, additional analysis independent of place fields' detection were performed (Geisler et al., 2007). These analysis also showed that in the presence of local cues individual cells' firing tended to oscillate faster than theta oscillation recorded in the LFP, a sign of theta phase precession while this was much less the case in the absence of local cues. Interestingly theta frequency speed modulation was strongly attenuated in the absence of local cues but normal in the presence of local cues while theta amplitude vs speed modulation was equivalent in both conditions. A similar absence of theta frequency vs speed modulation (with intact theta amplitude vs speed modulation) was observed in rats navigating virtual reality environments in the absence of local visual cues (Ravassard et al., 2013). However, in that case theta phase precession was unaffected. The absence of theta phase precession in mice in our recordings could reflect increased dependence on local cues for temporal coding in mice compared to rats (Hok et al., 2016; Kentros et al., 2004).

Altogether, our results show that coding in the absence of local visual cues corresponds to coding at low spatial resolution with a low number of spatially modulated cells, larger firing fields, decreased spatial selectivity and stability and poor theta phase precession. However, local visual cues increase spatial coding resolution both locally and globally. The use of virtual reality raises a growing interest in the field of neuroscience to study spatial cognition in rodents but also in non-human and human primates (Epstein et al., 2017). Our results suggest that enriching these environments with local visual cue could help comparing spatial coding in real and virtual environments. What would be the benefit of locally increasing spatial resolution? In the wild, rodents can travel kilometers away from their home to food locations through empty fields (Taylor, 1978). Mapping all parts of explored environment at high resolution would require a very large number of neurons and computational power (Geva-Sagiv et al., 2015). Accordingly, place fields tend to be larger in bigger environments (Fenton et al., 2008). Thus there might be a computational benefit to be able to map at high resolution important places like home base or food locations and to map lower resolution long transition routes between those locations (Geva-Sagiv et al., 2015). Such resolution could depend on the number of local sensory information as presented here. Future work should decipher whether increased spatial coding resolution is associated with better navigational accuracy and spatial memory.

References

Aghajan, Z.M., Acharya, L., Moore, J.J., Cushman, J.D., Vuong, C., and Mehta, M.R. (2015). Impaired spatial selectivity and intact phase precession in two-dimensional virtual reality. Nat. Neurosci. *18*, 121–128.

Aronov, D., and Tank, D.W. (2014). Engagement of Neural Circuits Underlying 2D Spatial Navigation in a Rodent Virtual Reality System. Neuron *84*, 442–456.

Barry, C., Lever, C., Hayman, R., Hartley, T., Burton, S., O'Keefe, J., Jeffery, K., and Burgess, N. (2006). The Boundary Vector Cell Model of Place Cell Firing and Spatial Memory. Rev. Neurosci. *17*, 71–97.

Battaglia, F.P. (2004). Local Sensory Cues and Place Cell Directionality: Additional Evidence of Prospective Coding in the Hippocampus. J. Neurosci. *24*, 4541–4550.

Brown, E.N., Frank, L.M., Tang, D., Quirk, M.C., and Wilson, M. a (1998). A statistical paradigm for neural spike train decoding applied to position prediction from ensemble firing patterns of rat hippocampal place cells. J. Neurosci. *18*, 7411–7425.

Burke, S.N., Maurer, A.P., Nematollahi, S., Uprety, A.R., Wallace, J.L., and Barnes, C.A. (2011). The influence of objects on place field expression and size in distal hippocampal CA1. Hippocampus *21*, 783–801.

Cabral, H.O., Fouquet, C., Rondi-Reig, L., Pennartz, C.M.A., and Battaglia, F.P. (2014). Single-Trial Properties of Place Cells in Control and CA1 NMDA Receptor Subunit 1-KO Mice. J. Neurosci. *34*, 15861–15869.

Chen, G., King, J.A., Burgess, N., and O'Keefe, J. (2013). How vision and movement combine in the hippocampal place code. Proc. Natl. Acad. Sci. *110*, 378–383.

Cohen, J.D., Bolstad, M., and Lee, A.K. (2017). Experience-dependent shaping of hippocampal CA1 intracellular activity in novel and familiar environments. Elife *6*, 1–27.

Cressant, A., Muller, R.U., and Poucet, B. (1997). Failure of Centrally Placed Objects to Control the Firing Fields of Hippocampal Place Cells. J. Neurosci. *17*, 2531–2542.

Danielson, N.B., Zaremba, J.D., Kaifosh, P., Bowler, J., Ladow, M., and Losonczy, A. (2016). Sublayer-Specific Coding Dynamics during Spatial Navigation and Learning in Hippocampal Area CA1. Neuron *91*, 652–665.

Deshmukh, S.S., and Knierim, J.J. (2011). Representation of Non-Spatial and Spatial Information in the Lateral Entorhinal Cortex. Front. Behav. Neurosci. *5*, 69.

Deshmukh, S.S., and Knierim, J.J. (2013). Influence of local objects on hippocampal representations: Landmark vectors and memory. Hippocampus *23*, 253–267.

509 Domnisoru, C., Kinkhabwala, A.A., and Tank, D.W. (2013). Membrane potential dynamics of
510 grid cells. Nature *495*, 199–204.
511
512 Dupret, D., O'Neill, J., Pleydell-Bouverie, B., and Csicsvari, J. (2010). The reorganization and
513 reactivation of hippocampal maps predict spatial memory performance. Nat. Neurosci. *13*,
514 995–1002.
515
516 Epstein, R.A., Patai, E.Z., Julian, J.B., and Spiers, H.J. (2017). The cognitive map in humans:
517 Spatial navigation and beyond. Nat. Neurosci. *20*, 1504–1513.
518
519 Fenton, A.A., Kao, H.-Y., Neymotin, S.A., Olypher, A., Vayntrub, Y., Lytton, W.W., and Ludvig,
520 N. (2008). Unmasking the CA1 Ensemble Place Code by Exposures to Small and Large
521 Environments: More Place Cells and Multiple, Irregularly Arranged, and Expanded Place
522 Fields in the Larger Space. J. Neurosci. *28*, 11250–11262.
523
524 Geiller, T., Fattahi, M., Choi, J.S., and Royer, S. (2017). Place cells are more strongly tied to
525 landmarks in deep than in superficial CA1. Nat. Commun. *8*, 14531.
526
527 Geisler, C., Robbe, D., Zugaro, M., Sirota, A., and Buzsaki, G. (2007). Hippocampal place cell
528 assemblies are speed-controlled oscillators. Proc. Natl. Acad. Sci. U. S. A. *104*, 8149–8154.
529
530 Geva-Sagiv, M., Las, L., Yovel, Y., and Ulanovsky, N. (2015). Spatial cognition in bats and rats:
531 From sensory acquisition to multiscale maps and navigation. Nat. Rev. Neurosci. *16*, 94–108.
532
533 Grienberger, C., Milstein, A.D., Bittner, K.C., Romani, S., and Magee, J.C. (2017). Inhibitory
534 suppression of heterogeneously tuned excitation enhances spatial coding in CA1 place cells.
535 Nat. Neurosci. *20*, 417–426.
536
537 Hartley, T., Burgess, N., Lever, C., Cacucci, F., and O'Keefe, J. (2000). Modeling place fields in
538 terms of the cortical inputs to the hippocampus. Hippocampus *10*, 369–379.
539
540 Harvey, C.D., Collman, F., Dombeck, D.A., and Tank, D.W. (2009). Intracellular dynamics of
541 hippocampal place cells during virtual navigation. Nature *461*, 941–946.
542
543 Hetherington, P.A., and Shapiro, M.L. (1997). Hippocampal place fields are altered by the
544 removal of single visual cues in a distance-dependent manner. Behav. Neurosci. *111*, 20–34.
545
546 Hirase, H., Czurkó, A., Csicsvari, J., and Buzsáki, G. (1999). Firing rate and theta-phase coding
547 by hippocampal pyramidal neurons during "space clamping." Eur. J. Neurosci. *11*, 4373–
548 4380.
549
550 Hok, V., Poucet, B., Duvelle, É., Save, É., and Sargolini, F. (2016). Spatial cognition in mice and
551 rats: similarities and differences in brain and behavior. Wiley Interdiscip. Rev. Cogn. Sci. *7*,
552 406–421.
553
554 Hollup, S. a, Molden, S., Donnett, J.G., Moser, M.B., and Moser, E.I. (2001). Accumulation of
555 hippocampal place fields at the goal location in an annular watermaze task. J. Neurosci. *21*,

1635–1644.

Holscher, C. (2005). Rats are able to navigate in virtual environments. J. Exp. Biol. *208*, 561–569.

Kentros, C.G., Agnihotri, N.T., Streater, S., Hawkins, R.D., and Kandel, E.R. (2004). Increased attention to spatial context increases both place field stability and spatial memory. Neuron *42*, 283–295.

Knierim, J.J., and Hamilton, D.A. (2011). Framing spatial cognition: neural representations of proximal and distal frames of reference and their roles in navigation. Physiol Rev *91*, 1245–1279.

Knierim, J.J., and Rao, G. (2003). Distal landmarks and hippocampal place cells: Effects of relative translation versus rotation. Hippocampus *13*, 604–617.

Marchette, S.A., Vass, L.K., Ryan, J., and Epstein, R.A. (2014). Anchoring the neural compass: Coding of local spatial reference frames in human medial parietal lobe. Nat. Neurosci. *17*, 1598–1606.

McGinley, M.J., Vinck, M., Reimer, J., Batista-Brito, R., Zagha, E., Cadwell, C.R., Tolias, A.S., Cardin, J.A., and McCormick, D.A. (2015). Waking State: Rapid Variations Modulate Neural and Behavioral Responses. Neuron *87*, 1143–1161.

McNaughton, B.L., Battaglia, F.P., Jensen, O., Moser, E.I., and Moser, M.B. (2006). Path integration and the neural basis of the "cognitive map." Nat Rev Neurosci *7*, 663–678.

van der Meer, M.A.A., Johnson, A., Schmitzer-Torbert, N.C., and Redish, A.D. (2010). Triple dissociation of information processing in dorsal striatum, ventral striatum, and hippocampus on a learned spatial decision task. Neuron *67*, 25–32.

Middleton, S.J., and McHugh, T.J. (2016). Silencing CA3 disrupts temporal coding in the CA1 ensemble. Nat. Neurosci. *19*, 945–951.

Mizuseki, K., Sirota, A., Pastalkova, E., and Buzsáki, G. (2009). Theta Oscillations Provide Temporal Windows for Local Circuit Computation in the Entorhinal-Hippocampal Loop. Neuron *64*, 267–280.

Muller, R.U., and Kubie, J.L. (1987). The effects of changes in the environment on the spatial firing of hippocampal complex-spike cells. J. Neurosci. *7*, 1951–1968.

Muller, R.U., Kubie, J.L., and Ranck, J.B. (1987). Spatial firing patterns of hippocampal complex-spike cells in a fixed environment. J. Neurosci. *7*, 1935–1950.

O' Keefe, J., and Burgess, N. (1996). Geometric determinants of the place fields of hippocampal neurons. Nature *381*, 425–428.

O'Keefe, J. (1976). Place units in the hippocampus of the freely moving rat. Exp. Neurol. *51*, 78–109.

O'Keefe, J., and Conway, D.H. (1978). Hippocampal place units in the freely moving rat: why they fire where they fire. Exp Brain Res *31*, 573–590.

O'Keefe, J., and Dostrovsky, J. (1971). The hippocampus as a spatial map. Preliminary evidence from unit activity in the freely-moving rat. Brain Res *34*, 171–175.

O'Keefe, J., and Nadel, L. (1978). The hippocampus as a cognitive map. (Oxford: Clarendon: Oxford University Press).

O'Keefe, J., and Recce, M.L. (1993). Phase relationship between hippocampal place units and the EEG theta rhythm. Hippocampus *3*, 317–330.

Pfeiffer, B.E., and Foster, D.J. (2013). Hippocampal place-cell sequences depict future paths to remembered goals. Nature *497*, 74–79.

Poucet, B., Chaillan, F., Truchet, B., Save, E., Sargolini, F., and Hok, V. (2015). Is there a pilot in the brain? Contribution of the self-positioning system to spatial navigation. Front. Behav. Neurosci. *9*, 1–10.

Ravassard, P., Kees, A., Willers, B., Ho, D., Aharoni, D., Cushman, J., Aghajan, Z.M., and Mehta, M.R. (2013). Multisensory control of hippocampal spatiotemporal selectivity. Science *340*, 1342–1346.

Renaudineau, S., Poucet, B., and Save, E. (2007). Flexible use of proximal objects and distal cues by hippocampal place cells. Hippocampus *17*, 381–395.

Rich, P.D., Liaw, H.P., and Lee, A.K. (2014). Large environments reveal the statistical structure governing hippocampal representations. Science *345*, 814–817.

Sato, M., Mizuta, K., Islam, T., Kawano, M., Gomez-Dominguez, D., Kim, K., Yamakawa, H., Ohkura, M., Fukai, T., Nakai, J., et al. (2018). Dynamic embedding of salience coding in hippocampal spatial maps. bioRxiv.

Schlesiger, M.I., Cannova, C.C., Boublil, B.L., Hales, J.B., Mankin, E.A., Brandon, M.P., Leutgeb, J.K., Leibold, C., and Leutgeb, S. (2015). The medial entorhinal cortex is necessary for temporal organization of hippocampal neuronal activity. Nat. Neurosci. *18*, 1123–1132.

Schmidt, R., Diba, K., Leibold, C., Schmitz, D., Buzsaki, G., and Kempter, R. (2009). Single-Trial Phase Precession in the Hippocampus. J. Neurosci. *29*, 13232–13241.

Schmidt-Hieber, C., and Häusser, M. (2013). Cellular mechanisms of spatial navigation in the medial entorhinal cortex. Nat. Neurosci. *16*, 325–331.

Shapiro, M.L., Tanila, H., and Eichenbaum, H. (1997). Cues that hippocampal place cells

650 encode: Dynamic and hierarchical representation of local and distal stimuli. Hippocampus *7*,
651 624–642.
652
653 Sheynikhovich, D., Chavarriaga, R., Strösslin, T., Arleo, A., and Gerstner, W. (2009). Is There a
654 Geometric Module for Spatial Orientation? Insights From a Rodent Navigation Model.
655 Psychol. Rev. *116*, 540–566.
656
657 Skaggs, W.E., McNaughton, B.L., Wilson, M.A., and Barnes, C.A. (1996). Theta phase
658 precession in hippocampal neuronal populations and the compression of temporal
659 sequences. Hippocampus *6*, 149–172.
660
661 Spiers, H.J., Hayman, R.M.A., Jovalekic, A., Marozzi, E., and Jeffery, K.J. (2015). Place field
662 repetition and purely local remapping in a multicompartment environment. Cereb. Cortex
663 *25*, 10–25.
664
665 Strösslin, T., Sheynikhovich, D., Chavarriaga, R., and Gerstner, W. (2005). Robust self-
666 localisation and navigation based on hippocampal place cells. Neural Networks *18*, 1125–
667 1140.
668
669 Taylor, K.D. (1978). Range of Movement and Activity of Common Rats (Rattus Norvegicus)
670 on Agricultural. J. Appl. Ecol. *15*, 663–677.
671
672 Tolman, E.C. (1948). Cognitive maps in rats and men. Psychol. Rev. *55*, 189–208.
673 Wiener, S.I., Paul, C.A., and Eichenbaum, H.B. (1989). Spatial and behavioral correlates of
674 hippocampal neuronal activity. J. Neurosci. *9*, 2737–2763.
675
676 Wilson, M., and McNaughton, B. (1993). Dynamics of the hippocampal ensemble code for
677 space. Science *261*, 1055–1058.
678
679 Youngstrom, I.A., and Strowbridge, B.W. (2012). Visual landmarks facilitate rodent spatial
680 navigation in virtual reality environments. Learn. Mem. *19*, 84–90.
681
682 Zhang, K., Ginzburg, I., McNaughton, B.L., and Sejnowski, T.J. (1998). Interpreting neuronal
683 population activity by reconstruction: unified framework with application to hippocampal
684 place cells. J. Neurophysiol. *79*, 1017–1044.
685

Supplementary Material and Methods

Animals

All experiments were approved by the Institut National de la Santé et de la Recherche Médicale (INSERM) animal care and use committee and authorized by the Ministère de l'Education Nationale de l'Enseignement Supérieur et de la Recherche (agreement number 02048.02), in accordance with the European community council directives (2010/63/UE).

Data were acquired from 8 male mice C57BL/6J (Janvier/Charles River) between 8 and 12 weeks during the recording phase (weight: 21 – 23.6 g). The mice were housed 2 or 3 per cages before the first surgery and then individually with 12 h inverted light/dark cycles. Trainings and recordings occurred during the dark phase.

Surgical procedure to prepare head fixation

A first surgery was performed to implant a fixation bar later used for head-fixation. Animals were anesthetized with isoflurane (3%) before intraperitoneal injection of ketamine (100 mg/Kg) mixed with xylazine (10 mg/Kg) supplemented with a subcutaneous injection of buprenorphine (0.06 mg/Kg). Two jeweller's screws were inserted into the skull above the cerebellum to serve as reference and ground. A dental cement hat was then constructed leaving the skull above the hippocampi free to perform the craniotomies later on. The free skull was covered with a layer of agarose 2% (wt/vol) and sealed with silicon elastomer (Kwik-Cast, World Precision Instruments). A small titanium bar (0.65 g; 12 x 6 mm) was inserted in the hat above the cerebellum to serve as a fixation point for a larger head plate used for head fixation only during training and recordings.

Virtual reality set up

A commercially available virtual reality system (Phenosys Jetball-TFT) was combined with a custom designed 3D printed concave plastic wheel (center diameter: 12.5 cm; side diameter: 7.5 cm; width: 14 cm, covered with silicon-based white coating) to allow 1D movement with a 1/1 coupling between movement of the mouse on the wheel and movement of its avatar in the virtual reality environment. This solution was preferred to the original spherical treadmill running in a X-only mode (which takes into account only rotations of the ball in the

X axis to actualize the position of the avatar in the virtual reality environment) which also allows 1D movement but with a more variable coupling between movement of the mouse on the treadmill and its avatar in the virtual reality environment. The wheel was surrounded by six 19-inches TFT monitors, which altogether covered a 270 degrees angle. Monitors were elevated so that the mice's eyes level corresponded to the lower third of the screen height to account for the fact that rodents field of view is biased upward. The head fixation system (Luigs and Neumann) was located behind the animal to not interfere with the display of the virtual reality environment. The virtual reality environment was a virtual 200 cm long and 32 cm wide linear maze with different patterns on the side and end walls and virtual 3D objects (see virtual reality environment section). Movement of the wheel actualized the mouse's avatar position. The mouse could only perform forward or backward movements but could not turn back in the middle of the track (see training section).

Virtual reality environments

No Object Track (ØT)

Each side wall had a unique pattern (black and orange stripes on one wall; green crosses on black background on the other wall). End-walls had grey triangular or round shapes on a yellow background (Fig. 1A).

Object Track (OT)

This maze was identical to the ØT maze concerning wall patterns and dimensions but 3 virtual objects were included on the sides between the animal trajectory and the walls (Fig. 1A). The objects were a yellow origami crane (dimensions: 9 x 9 x 7 cm; position: 37 cm from end wall), a blue and grey cube (dimensions: 5 x 5 x 5 cm; position: 64 cm from end wall) and a tree (15 x 15 x 22 cm; position: 175 cm from end-wall). The animal could neither orient toward the objects nor get any sensory feedback from them by any other mean but vision.

Enriched Objects Track (EOT)

This maze had the same dimensions as previous mazes and included the same virtual reality objects (identical dimensions and locations than in the previous maze) but the side walls had distinct symmetrical patterns in different locations along the maze (50 cm long; black dots on white background, black and green squares, black and white stripes and green crosses on black background). Outside the maze walls, two large 3D columns were positioned on each

side (dimensions 8 x 8 x 47 cm; positions 58 and 143 cm from end wall) to provide additional visual cues.

Training

Mice were first habituated to the experimentalist through daily handling sessions of 20 min or more that continued throughout the experiment. After a 3 days post-surgery recovery period, mice were water-deprived (1 ml/day, including the quantity of water taken during the training). After 2-3 days of water deprivation, they were progressively trained to run in the virtual reality set up. First, mice were familiarized with running head-fixed on the wheel for water rewards in a black track (screens always black). During these sessions, animals received as a reward sweetened water (5% sucrose) for each 50 centimeters ran on the wheel. Once the animal was comfortable with the setup, it was trained to run in one of three linear virtual tracks (familiar track). When animals reached the end of the track, a liquid reward delivery tube extended in front of the animal and animal had to lick to get the reward (a 4 µL drop of water of 5% sucrose). Animals were then teleportated in the same position but facing the opposite direction of the maze and had to run up to the end of the maze in the opposite direction to get another reward. Animals were initially trained during 15 minutes sessions. Session time was progressively increased to reach 60 minutes. *Ad libidum* water access was restored if the weight of the animal decreased beneath 80% of the pre-surgery weight at any stage during training.

Recording procedure

When animals reached a stable behavioral performance (at least 1 reward/minute during 60 minutes), we performed acute recordings using silicon probes (4/8 shanks; A-32/A-64 Buzsaki Probe, Neuronexus). On the day before recording, animals were anesthetized (induction: isoflurane 3%; maintenance: Xylazine/Ketamine 10/100 mg/Kg supplemented with Buprenorphine 0.1 mg/Kg) and a craniotomy was drilled above one hippocampus (centered on a location -2 mm posterior and ± 2.1 mm lateral from bregma). The craniotomy was covered with agarose (2% in physiological saline) then sealed with silicon elastomer (Kwik-Cast, World Precision Instruments). On the day of the recording the backside of the probe's shanks was covered with a thin layer of a cell labeling red-fluorescent dye (DiI, Life

A

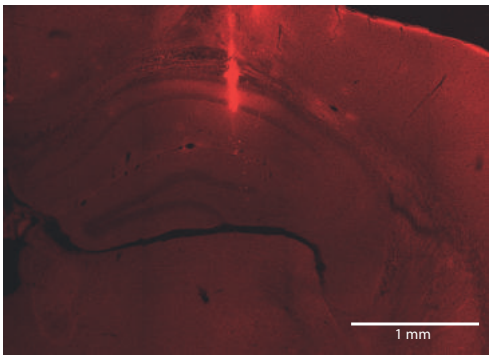

B

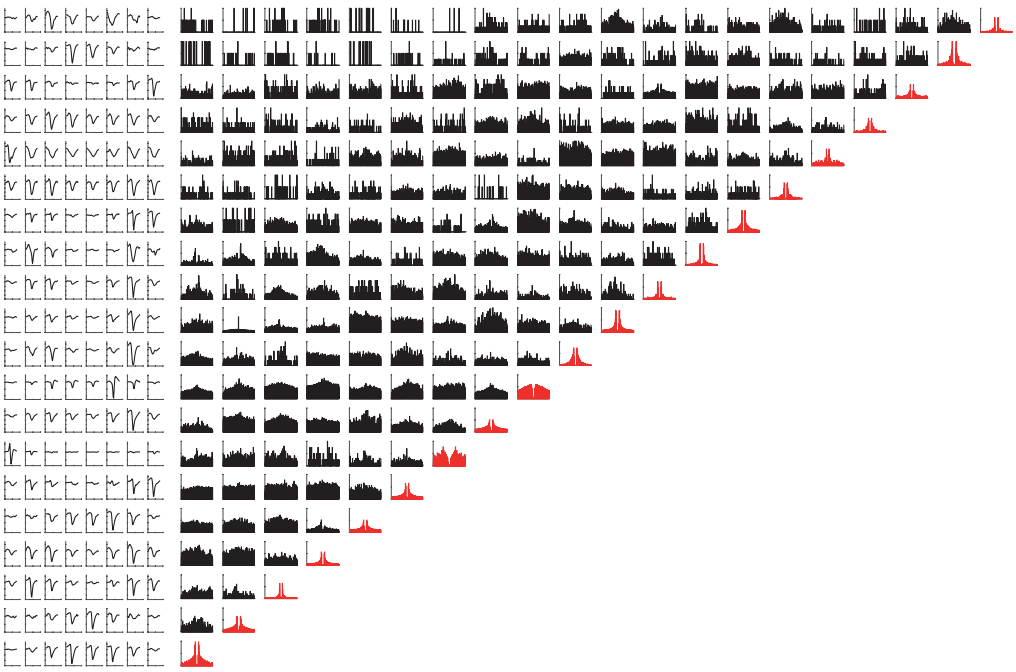

Supplementary Figure 1: Histology and spike sorting

A. Representative histology slide showing a silicon probe track ending in CA1 pyramidal layer. Scale bar: 1mm. **B.** (Right) Auto-correlograms (red) and cross-correlograms (black) of 20 CA1 units recorded simultaneously. (Left) Average units waveforms (for visualization each row is normalized by the unit maximum average waveform)

779 technologies) so that the location of the recording sides (tips of the shanks) could be
780 assessed post-hoc histologically. The silicon probe was then lowered into the brain while the
781 animal was allowed to walk freely on the wheel with the screens displaying a black
782 background. The good positioning of the probe with recording sites in the CA1 pyramidal cell
783 layer was verified by the presence of multiple units showing complex spike bursts on several
784 recordings sites and the recording of sharp-wave ripples during quiet behavior. After
785 positioning of the silicon probe the virtual reality environment was displayed on the screen.
786 All mice (n = 8) experienced first the familiar environment (either ØT, OT or EOT) for around
787 20 back and forth trials. For mice trained in ØT or OT (n = 3 and 2, respectively), this first
788 exploration was followed, after 3 minutes of free running with the screens displaying a black
789 background, by exploration of a new environment, identical to the previous one except for
790 the presence of the three 3D objects (objects were added for mice trained in ØT and
791 removed for mice trained in OT) for another 20 consecutive back and forth trials. For some
792 of these mice (n = 2 for EOT, n = 1 for OT and n = 2 for ØT) sessions in the familiar track and
793 novel track were divided into two sub-sessions interleaved by 3 min of free running with the
794 screens black. The two sub-sessions in the familiar environment and the new environment
795 were pulled together for analysis. Note that animals stayed head-fixed on the wheel
796 surrounded by screens during the entire recoding session.
797

798 **Data Acquisition and Pre-Processing**

799 The position of the animal in the virtual maze was digitalized by the virtual reality controlling
800 computer (Phenosys) and then sent to a digital-analog card (0-4.5V, National Instrument
801 Board NI USB-6008) connected to the external board (I/O Board, Open Ephys) of a 256
802 channels acquisition board (Open Ephys). Neurophysiological signals were acquired
803 continuously on a 256-channels recording system (Open Ephys, Intan Technologies,
804 RHD2132 amplifier board with RHD2000 USB interface board) at 25,000 Hz. Spike sorting
805 was performed semi-automatically using KlustaKwik (https://github.com/klusta-
806 team/klustakwik). Clusters were then manually refined using cluster quality assessment,
807 auto- and cross-correlograms, clusters waveforms and similarity matrix (Klustaviewa,
808 Rossant et al., 2016).
809

Data Analysis

All subsequent analyses were conducted using custom-developed softwares written in MATLAB (MathWorks).

Reward & Object Zones Definition

The reward zones, located between the maze extremities and 10% of the track length (0-20 cm and 180-200 cm), were not considered in the analysis. The object zone was composed of two zones, one from 30 to 70 cm including both the origami crane and the cube and the other from 160 to 180 cm including the tree.

Firing Rate Map

The maze was divided into 100 spatial bins measuring 2 cm. For each trial, the number of spikes and the occupancy time of the animal in each spatial bin were calculated to obtain the spikes number vector and the occupancy time vector, respectively. These vectors were smoothed using a Gaussian filter with a half-width set to 10 spatial bins. Spikes occurring during epochs when velocity was lower than 2 cm/s were removed from all analysis. The smoothed spikes number vector was divided by the smoothed occupancy time vector to obtain the firing rate vector for each trial. The firing rate vectors were pooled for a specific condition (e.g., Familiar Objects Track) and direction of the animal (e.g., back) to generate a firing rate map. These pooled vectors were also averaged to provide the mean firing rate vector, corresponding to the mean firing rate for each spatial bin.

Pyramidal Cell Classification

Cells with a mean firing rate lower than 20 Hz and either a burst index (Royer et al., 2012) greater than 0 or the spike duration greater than 0.4 ms were classified as putative pyramidal neurons. They were classified as interneurons otherwise.

Active Cells Classification

A cell was considered as active when the mean firing rate was greater than 0.5 Hz, the peak firing rate was greater than 1.5 Hz and the cell fired at least one spike in 50% of the trials. These 3 criteria had to be verified in either the forth or back direction.

Place Fields Detection

To detect a mean place field, a bootstrap procedure was performed. For each trial, a new spikes train was generated using a Poisson process with λ equal to the mean firing rate of the trial and a 1 ms time interval. A “randomized” firing rate map was then generated and the mean firing rate vector was determined and compared with the mean firing rate vector

from the initial rate map. This operation was repeated 1000 times to determine a *P*-value vector (*P*-value for each 2 cm spatial bin). Place fields candidates were defined as a set of more than 3 continuous spatial bins associated with *P*-values lower than 0.01. Two place fields were merged when the distance between their closest edges was at most equal to 5 spatial bins (10 cm). Place fields' edges were extended by at most 5 spatial bins (for each edge) when the *P*-value was below 0.30 for these bins. A field with a size greater than 45 spatial bins (90 cm) was not considered as a place field. To validate a mean place field, the cell had to verify a stability criterion. Spatial correlations were calculated between the firing rate vector of each trial and the mean firing rate vector. The spatial bins corresponding to other detected place fields were not considered in the spatial correlations. The place field was validated if the spatial correlations were greater than 0.60 for at least 40% of trials. Unless specified, when several mean place fields were detected, only the place field with the highest peak was conserved. An active cell with at least one place field in one direction was considered as a place cell.

The same procedure was applied to detect place fields per lap without the stability criterion, which cannot be calculated on single trials. A place field per lap was conserved if it overlapped at least 1 spatial bin with the closest mean place field.

Stability Index

The stability index of a cell was computed as the mean of the spatial correlations between all pairs of firing rate vectors. This way, the cell stability index takes into account the activity patterns from all the trials and provides a reliable quantification of the inter-trial reproducibility of the cells activity. Note that this stability index is different from usual stability indexes based on correlations of mean firing rates between even and odd trials or two halves of the same recording session thus values obtained cannot be directly compared.

Spatial Information

The spatial information (SI) was calculated according to the following formula(Skaggs et al., 1996):

$$SI = \sum_{i=1}^{N} \left[\frac{FR_i}{\overline{FR}} \times \frac{OT_i}{OT_T} \times log_2 \left(\frac{FR_i}{\overline{FR}} \right) \right]$$

where N is the number of spatial bins (N = 100), FR_i is the mean firing rate determined in the i-th spatial bin, $\overline{FR}$ is the mean firing rate, OT_i is the mean occupancy time determined

in the i-th spatial bin, OT_T is the total occupancy time based on the mean occupancy time vector.

Out/In Field Firing Rate

The out/in field firing rate was computed as the ratio between the mean firing rate outside the mean place field (excluding secondary place fields) and the mean firing rate inside the mean place field.

Place Field Dispersion

A place field dispersion measure has been computed to quantify how much each place field per lap was dispersed around the mean place field. The place field dispersion (PFD) was calculated according to the following formula:

$$PFD = \frac{L}{N}\left[\frac{1}{M}\sum_{i=1}^{M}(C - C_i)^2\right]^{\frac{1}{2}}$$

Where C is the center of the mean place field, C_i is the center of the field in the i-th lap and M is the number of laps, L is the total length of the maze and N is the number of spatial bins. The center of a place field was defined as the spatial bin with the highest firing rate.

Place Field' Width

Place field' width was computed as the distance between the place field edges and only determined for entire place fields. A place field was considered as complete when its firing rate increased above 30% of the difference between highest and lowest place field activity and then dropped below this threshold.

On-Track and End-Track Fields

A mean place field was considered as End-Track field if the peak of the field was located at the beginning of the reward zone (i.e., at the 11-th or the 90-th spatial bin). All other fields were classified as On-Track fields.

Distribution of place fields' position

To statistically assess whether the place fields were non-uniformly distributed in the maze, we tested the null hypothesis that all fields were uniformly distributed. Based on this hypothesis, the total number of place fields was redistributed with an equal probability to be in each 10-cm spatial bin. The standard deviation of this uniform distribution was then compared to the initial distribution. This operation was repeated 1000 times (bootstrap procedure) to obtain a *P*-value, corresponding to the probability of the place fields to be

uniformly distributed. When this *P*-value was lower than 0.05, the null hypothesis was rejected and the distribution was considered as non-uniform. To ensure that single values of place fields' percentage in a given bin did not make the distribution non-uniform, values greater than the 93-th percentile and lower than the 6-th percentile have been excluded from the initial distribution.

Local Stability

A local stability index was developed to assess how consistent a firing rate was over the laps for a given spatial bin. To this end, two mean firing rate vectors were calculated, in the neighborhood of each spatial bin (2-spatial bins half-window) for even and odd trials. Local stability index was defined as the spatial correlation between these two vectors for a given spatial bin.

Position Decoding

To address how informative the firing rates of the CA1 pyramidal cells ensemble were about the position of the animal in the different virtual environments, we used Bayesian decoding and Firing Rate Vectors (FRV) methods. For each time window, the distribution of the animal position probability across the whole maze was calculated using the firing activity of all active cells (place cells and non place cells). The mode of this distribution (maximum of probability) was chosen as the decoded position for a given time window. We used a classical "memoryless" Bayesian decoder (Brown et al., 1998; Zhang et al., 1998). The decoding of the spikes data was restricted to periods when the animal was running (speed > 2 cm/s) or with good Theta/Delta ratio (Jackson and Redish, 2007) and cross-validated using the "leave one out" approach. We computed the animal's probability to be in each spatial bin *x* (2 cm) knowing that N cells fired *n* spikes in a time window according to the following formula:

$$P(x|n) = C(\tau, \mathrm{n})\mathrm{P}(\mathrm{x})\left(\prod_{i=1}^{N} f_i(x)^{n_i}\right)\exp\left(-\tau\sum_{i=1}^{N} f_i(x)\right)$$

With *P(x)* a uniform spatial prior, $f_i(x)$ the average firing rate of the neuron *i* over *x* (i.e., the tuning curve over the position), n_i the number of spikes emitted by the neuron *i* in the current time window and τ the length of the time window (150 ms; non-overlapping) and $C(\tau, n)$ a normalization factor intended to set the posterior probability for one time window to 1. This formula assumes that the spikes trains obey to a Poisson process and that cells activity is independent. Position decoding was also preformed using the FRV method

(Middleton and McHugh, 2016). For each 100 ms time bin, the Pearson correlations were calculated between firing rates across all cells and the mean firing rates from all cells for a given spatial bin. A decoding error was defined as the absolute value of the difference between decoded and real position. Accuracy was defined as the probability at the real position in a particular time bin. To ensure that the position decoding was not influenced by the number of cells, a drop cell approach was performed (van der Meer et al., 2010). Briefly, for M recorded active cells, the position was decoded using k different subsets of cells with increasing sizes 5*k with k ranging from 1 to the last multiple of 5 < M. For the k-th subset, the decoding was repeated 50 times using 5*k randomly selected cells and the median value of probabilities for a given time and spatial bin was chosen as the final probability. The presented results were computed for a subset composed of 20 cells (k = 4).

Map Similarity over Trials

To analyze the dynamic of the changes of spatial representation between familiar and novel conditions, map similarities were performed for 10 back and forth trials before and after the experimental manipulation. For each active putative pyramidal cell, map similarities consisted of the Pearson correlation between the firing rate map of each back and forth trial and a template firing rate map. This template firing rate map was calculated as the average of the firing rate map from all the laps in the condition with objects (most stable condition). The maps corresponding to back (forth) trials were correlated to the mean back (forth) trial map in the object condition and the correlations values were averaged to obtain a single value for this back and forth trial. When map similarity was determined for a lap in the object condition, the template firing rate map was computed without it.

Landmark Vector cells detection

For this analysis, we defined individual objects zones (IOZ) for each object. For a given object, IOZ corresponded to all spatial bins occupied by the object plus an additional margin of 7 spatial bins (14 cm), which was always located before the object in the animals' movement reference frame to take into account the anticipatory nature of some LV cells(Geiller et al., 2017). Thus IOZ for each object were different for back and forth directions. Here are the IOZ defined for each object in both directions: origami crane: 20-42 cm and 32-56 cm, cube: 46-68 cm and 60-82 cm and tree 154-180 cm and 166-180 cm. Note that secondary mean place fields were included in this analysis (i.e. if multiple place fields

were detected, if at least one of theses place fields was in the same IOZ for both directions the cell was classified as a LV cell).

Phase precession Analysis

Phase precession was calculated on all spikes (above speed threshold) for the track with objects but restrained to Spatially Stable Trials (SST) in the no object condition to equalize stability between both conditions. SST consisted of at least 3 trials where the in-field correlation with the mean place field exceeded 0.6. To assess theta phase precession, the Local Field Potential (LFP) of the channel with the highest number of pyramidal cells(Skaggs et al., 1996) was filtered (4^{th} order Chebyshev filter type II) in the theta band (4-12Hz). The instantaneous theta phase for each time bin (1 ms) was determined using the Hilbert transform of the filtered LFP and a phase was attributed to each spike. Only theta phase locked cells were considered in the following analysis (non-uniform phase distribution, $P < 0.05$, Rayleigth test). Circular linear analysis was used to determine the correlation strength and slope value of the relation between spikes phases and normalized positions (0-1) through the mean place field (Kempter et al., 2012). Briefly, the phase precession slope was computed with a linear regression model between circular (spike phases) and linear (animal's position) data. The slope of the regression was used to scale the animal's position and to transform it into a circular variable. A circular-circular correlation could thus be computed on the data to assess the strength of the relationship between spike phases and animal's position. A significance value was determined by re-computing the correlation values for 1000 permutations of the spikes position.

Analysis of phase precession on single-trial detected fields was also performed (Schmidt et al., 2009). Phase precession slope and correlation values were computed similarly to the previously described method. The single lap slope and correlation values were averaged only for sessions with at least 3 significantly precessing trials where the cell emitted a minimum of 4 spikes inside the mean place field.

Unit-LFP shift and Spike Phase Spectrum

To quantify phase precession independently of the position of the animal and the place field detection, Unit-LFP shift was used. For all active putative pyramidal cells, a discreet multitaper spectrum in the theta band (4-12Hz) of the cell's spikes was performed (mtpointspectrum, Chronux) as well as the continuous multitaper spectrum of the simultaneously recorded LFP (mtspectrumc, Chronux). A theta modulation index (Mizuseki et

al., 2009) was defined for each cell spike spectrum as the mean power around the peak theta frequency ± 0.5 Hz divided by the mean power below 5Hz or above 9Hz. A cell was considered as theta modulated if this index was greater than 1.4. The cross correlogram was then calculated for theta modulated cells to determine the lag in the theta band between the LFP and the cells' spectrum (Geisler et al., 2007). A positive lag indicates that the cell is firing faster than the concurrent LFP.

Speed modulation of theta frequency and Amplitude

The instantaneous theta frequency was computed from the instantaneous theta phase extracted from the Hilbert transform of the filtered LFP in the theta band. For each time t_i, the instantaneous theta frequency ($F_{\theta}(t_i)$) was determined based on the unwrapped phase:

$$F_{\theta}(t_i) = \frac{Phase(t_{i+1}) - Phase(t_i)}{2\pi * Fs}$$

where *Fs* is the sampling frequency.

Instantaneous theta amplitude was defined as the module of the LFP Hilbert transform and normalized by the mean LFP theta amplitude. The Pearson correlation coefficient was then calculated between the speed of the animal and theta frequency/amplitude.

A theta peak detection method was also used to calculate the instantaneous theta frequency. Theta peaks were detected with zero crossing of the instantaneous LFP phase and frequency was deduced from the time between two successive theta peaks. This value was affected to all the time stamp of the corresponding cycle.

Statistics

All statistical analyses were conducted using Matlab codes (MathWorks). For each distribution, a Lilliefors goodness-of-fit test was used to verify if the data were normally distributed and a Levene test was used to assess for equal variance. If normality or equal variance were not verified, we used the Wilcoxon rank sum test or the Kruskal-Wallis test otherwise the Student t-test was used. Spatial correlations were computed using Pearson's correlation coefficient. Chi-square test was used to compare percentages.

Supplementary references

Brown, E.N., Frank, L.M., Tang, D., Quirk, M.C., and Wilson, M. a (1998). A statistical paradigm for neural spike train decoding applied to position prediction from ensemble firing patterns of rat hippocampal place cells. J. Neurosci. *18*, 7411–7425.

Geiller, T., Fattahi, M., Choi, J.S., and Royer, S. (2017). Place cells are more strongly tied to landmarks in deep than in superficial CA1. Nat. Commun. *8,* 14531.

Geisler, C., Robbe, D., Zugaro, M., Sirota, A., and Buzsaki, G. (2007). Hippocampal place cell assemblies are speed-controlled oscillators. Proc. Natl. Acad. Sci. U. S. A. *104*, 8149–8154.

Jackson, J., and Redish, A.D. (2007). Network dynamics of hippocampal cell-assemblies resemble multiple spatial maps within single tasks. Hippocampus *17*, 1209–1229.

Kempter, R., Leibold, C., Buzsáki, G., Diba, K., and Schmidt, R. (2012). Quantifying circular-linear associations: Hippocampal phase precession. J. Neurosci. Methods *207*, 113–124.

van der Meer, M.A.A., Johnson, A., Schmitzer-Torbert, N.C., and Redish, A.D. (2010). Triple dissociation of information processing in dorsal striatum, ventral striatum, and hippocampus on a learned spatial decision task. Neuron *67*, 25–32.

Middleton, S.J., and McHugh, T.J. (2016). Silencing CA3 disrupts temporal coding in the CA1 ensemble. Nat. Neurosci. *19*, 945–951.

Mizuseki, K., Sirota, A., Pastalkova, E., and Buzsáki, G. (2009). Theta Oscillations Provide Temporal Windows for Local Circuit Computation in the Entorhinal-Hippocampal Loop. Neuron *64*, 267–280.

Rossant, C., Kadir, S.N., Goodman, D.F.M., Schulman, J., Hunter, M.L.D., Saleem, A.B., Grosmark, A., Belluscio, M., Denfield, G.H., Ecker, A.S., et al. (2016). Spike sorting for large, dense electrode arrays. Nat. Neurosci. *19*, 634–641.

Royer, S., Zemelman, B. V., Losonczy, A., Kim, J., Chance, F., Magee, J.C., and Buzsáki, G. (2012). Control of timing, rate and bursts of hippocampal place cells by dendritic and somatic inhibition. Nat. Neurosci. *15*, 769–775.

Schmidt, R., Diba, K., Leibold, C., Schmitz, D., Buzsaki, G., and Kempter, R. (2009). Single-Trial Phase Precession in the Hippocampus. J. Neurosci. *29*, 13232–13241.

Skaggs, W.E., McNaughton, B.L., Wilson, M.A., and Barnes, C.A. (1996). Theta phase precession in hippocampal neuronal populations and the compression of temporal sequences. Hippocampus *6*, 149–172.

Zhang, K., Ginzburg, I., McNaughton, B.L., and Sejnowski, T.J. (1998). Interpreting neuronal population activity by reconstruction: unified framework with application to hippocampal place cells. J. Neurophysiol. *79*, 1017–1044.